

# Discrete Boltzmann multi-scale modeling of non-equilibrium multiphase flows

Yanbiao Gan<sup>1</sup>, Aiguo Xu<sup>2,3,4,†</sup>, Huilin Lai<sup>5</sup>, Wei Li<sup>1</sup>, Guanglan Sun<sup>1,6</sup>, and Sauro Succi<sup>7,8</sup>

<sup>1</sup>Hebei Key Laboratory of Trans-Media Aerial Underwater Vehicle, School of Liberal Arts and Sciences, North China Institute of Aerospace Engineering, Langfang 065000, China

<sup>2</sup>Laboratory of Computational Physics, Institute of Applied Physics and Computational Mathematics, P. O. Box 8009-26, Beijing 100088, China

<sup>3</sup>State Key Laboratory of Explosion Science and Technology, Beijing Institute of Technology, Beijing 100081, China

<sup>4</sup>HEDPS, Center for Applied Physics and Technology, and College of Engineering, Peking University, Beijing 100871, China

<sup>5</sup>College of Mathematics and Statistics, FJKLMAA, Center for Applied Mathematics of Fujian Province (FJNU), Fujian Normal University, Fuzhou 350117, China

<sup>6</sup>School of Physics, Beijing Institute of Technology, Beijing 100081, China

<sup>7</sup>Center for Life Nano Science at La Sapienza, Fondazione Istituto Italiano di Tecnologia, Viale Regina Margherita 295, 00161, Roma, Italy

<sup>8</sup>Physics Department and Institute for Applied Computational Science, John A. Paulson School of Applied Science and Engineering, Harvard University, Oxford Street 29, Cambridge, MA 02138, USA

(Received xx; revised xx; accepted xx)

The aim of this paper is twofold: the first is to formulate and validate a multi-scale discrete Boltzmann method (DBM) based on density functional kinetic theory for thermal multiphase flow systems, ranging from continuum to transition flow regime; the second is to present some new insights into the thermo-hydrodynamic non-equilibrium (THNE) effects in the phase separation process. Methodologically, DBM includes three main pillars: (i) the determination of the fewest kinetic moment relations, which are required by the description of significant THNE effects beyond the realm of continuum fluid mechanics, (ii) the construction of appropriate discrete equilibrium distribution function recovering all the desired kinetic moments, (iii) the detection, description, presentation and analysis of THNE based on the moments of the non-equilibrium distribution ( $f - f^{(eq)}$ ). The incorporation of appropriate additional higher-order thermodynamic kinetic moments considerably extends the DBM's capability of handling larger values of the liquid-vapor density ratio, curbing spurious currents, and ensuring mass-momentum-energy conservation. Compared with the DBM with only first-order THNE (Gan *et al.* 2015), the model retrieves kinetic moments beyond the third-order super-Burnett level,

† Email address for correspondence: Xu\_Aiguo@iapcm.ac.cn

and is accurate for weak, moderate, and strong THNE cases even when the local Knudsen number exceeds  $1/3$ . Physically, the ending point of the linear relation between THNE and the concerned physical parameter provides a distinct criterion to identify whether the system is near or far from equilibrium. Besides, the surface tension refrains the local THNE around the interface, but expands the THNE range and strengthens the THNE intensity away from the interface through interface smoothing and widening.

**Key words:** kinetic theory, discrete Boltzmann method, multi-scale modeling, thermo-hydrodynamic non-equilibrium effect, multiphase flow

---

## 1. Introduction

Multiphase flows with phase transitions and heat transfer are ubiquitous in natural and industrial processes, such as atmospheric phenomena, material and food processing, petrochemical engineering, bio-medical as well as life science (Brennen 2005; Zang *et al.* 2019; Bernaschi *et al.* 2019; Wu *et al.* 2021*b*). Therefore, establishing accurate, reliable and efficient models and computational strategies for predicting their flow behavior, will deepen our understanding of the fundamental and underlying physical mechanisms behind multiphase flows. Besides major academic significance as complex phenomena far from equilibrium, they also bear essential industrial value.

Nevertheless, multi-scale modeling and simulation of such a complex system is a long-standing challenge (Luo *et al.* 2009; Zang *et al.* 2019; Bernaschi *et al.* 2019). The challenge arises from the common and unique features of these fluids: (i) complex multi-scale structures and their cross-scale correlations, such as particles, bubbles, droplets and clusters; (ii) rich and abundant evolving interfaces, such as material and mechanical interfaces; (iii) complex forces, relaxations and responses, such as gradient forces, inter-particle forces, external forces, and the nonlinear coupling among them; (iv) competition between various spatiotemporal scales and kinetic modes, such as growth, deformation, breakup, cavitating, boiling, and even turbulence.

In general, a multiphase flow system is in a global or local thermo-hydrodynamic non-equilibrium (THNE) state with fluctuations (Parsa & Wagner 2020), including significant hydrodynamic and thermodynamic non-equilibrium (HNE and TNE, respectively) effects which may undermine the validity of macroscopic models, such as the most commonly used Navier-Stokes (NS) equations. Simplifying assumptions, such as thermal equilibrium across a liquid-vapor interface during phase separation can lead to erroneous predictions (Persad & Ward 2016). A possible solution for accessing detailed THNE effects is to use particle-based methods, for example, molecular dynamics or direct simulation Monte Carlo method (Liu *et al.* 2017, 2020). However, the spatiotemporal scales and

geometries that the two schemes can afford are extremely small and highly idealized compared with those of practical applications.

As a mesoscopic approach and a natural bridge connecting microscopic and macroscopic models, suitably extended versions of the Boltzmann equation can in principle describe the complex non-equilibrium thermo-hydrodynamics for the full spectrum of flow regimes (Chapman & Cowling 1990). However, the nonlinearity, multidimensionality, and integro-differential nature of the collision term pose a formidable challenge to its direct solution. The difficulty in using the original Boltzmann equation has prompted the development of approximate and simplified kinetic models that relinquish much of its computational complexity while preserving its most relevant physics in point. The versatile lattice Boltzmann method (LBM) (Benzi *et al.* 1992; Chen & Doolen 1998; Wagner & Yeomans 1998; Succi 2001, 2018; Zheng *et al.* 2006; Sbragaglia *et al.* 2007; Xu *et al.* 2012; Guo & Shu 2013; Bernaschi *et al.* 2019; Huang *et al.* 2021a; Falcucci *et al.* 2021; Wei *et al.* 2022; Bhairapurada *et al.* 2022) and the recently developed discrete Boltzmann modeling method (DBM) (Gan *et al.* 2015; Lai *et al.* 2016; Lin *et al.* 2017; Gan *et al.* 2018, 2019; Zhang *et al.* 2019; Chen *et al.* 2020; Zhang *et al.* 2021; Xu *et al.* 2021a,b,c), belong precisely to this class of modern non-equilibrium methods.

As for the LBM research, there are two complementary branches. The first is a physics-inspired construction method, while the second is a numerical scheme for solving partial differential equation(s), such as wave equation (Yan 2000; Lai & Ma 2011), convection-diffusion equation (Shi & Guo 2009; Du & Liu 2020; Chen *et al.* 2021b), Poisson equation (Chai & Shi 2008), Laplace equation (Zhang *et al.* 2009), Fisher equation (Succi 2014), Burgers equation (Elton 1996; Duan & Liu 2007; Liu & Shi 2011), Benjamin-Ono equation (Lai & Ma 2010), Korteweg-de Vries equation (Lan *et al.* 2019; Wang 2017b), Klein-Gordon-Zakharov equation (Wang 2019), Zakharov-Kuznetsov equation (Wang 2017a, 2020), Ginzburg-Landau equation (Zhang & Yan 2010, 2014), Kuramoto-Sivashinsky equation (Lai & Ma 2009; Otomo *et al.* 2018), Schrödinger equation (Succi 2001; He & Lin 2020), etc. These two branches build on similar, yet not equal, construction rules. DBM was developed from the first branch and represents a mesoscopic modeling method for fluid flows.

Although the original Boltzmann equation and its approximations work only for dilute gas systems, they can be extended to multiphase flow regimes after incorporating the non-ideal gas effects through a variety of approaches. Actually, both LBM and DBM are particularly promising in the area of multiphase and multicomponent flows, mainly on account of their kinetic nature, directly inherited from the Boltzmann equation, which facilitates the inclusion of microscopic physical interactions as compared to numerical methods based on continuum models.

To date, many LBMs for multiphase flows have been proposed, including the chromodynamic model Gunstensen *et al.* (1991), the pseudo-potential model (Shan & Chen

1993, 1994), the free-energy model (Swift *et al.* 1995, 1996; Xu *et al.* 2003, 2004), the kinetic-theory-based model (He *et al.* 1998, 1999a), the forcing model (Sofonea *et al.* 2004; Gonnella *et al.* 2007), the phase-field model (Rasin *et al.* 2005), the entropic kinetic model (Mazloomi M *et al.* 2015; Montessori *et al.* 2017; Wöhrwag *et al.* 2018), the unified collision model (Luo *et al.* 2021), and so forth. Although proposed from different perspectives, the common point of these models is the inclusion of interparticle interactions at the mesoscopic scale. The interparticle interactions are the underlying engine behind the complex THNE features of multiphase flows. The aforementioned models and their revised versions have been successfully applied to the study of fundamental phenomena and mechanisms of multiphase flows in science and engineering, ranging from droplet evaporation (Ledesma-Aguilar *et al.* 2014; Safari *et al.* 2013, 2014; Zarghami & Van den Akker 2017; Qin *et al.* 2019), to droplet deformation, breakup, splashing, and coalescence (Wagner *et al.* 2003; Wang *et al.* 2015a,b; Chen & Deng 2017; Liu *et al.* 2018; Liang *et al.* 2019; Wen *et al.* 2017, 2020), collapsing cavitation (Chen *et al.* 2011; Falcucci *et al.* 2013; Kähler *et al.* 2015; Sofonea *et al.* 2018; Yang *et al.* 2020, 2022), acoustics levitation (Zang 2020), nucleate boiling (Li *et al.* 2016, 2018; Fei *et al.* 2020), ferrofluid and electro-hydrodynamic flows (Falcucci *et al.* 2009; Hu *et al.* 2018; Liu *et al.* 2019), hydrodynamic instability (He *et al.* 1999b; Zhang *et al.* 2001; Fakhari & Lee 2013; Liang *et al.* 2014, 2016a,b; Tavares *et al.* 2021), dendritic growth (Rasin *et al.* 2005; Rojas *et al.* 2015; Sun *et al.* 2016a,b), heat and mass transfer in porous media (Chen *et al.* 2015; Liu *et al.* 2016; He *et al.* 2019; Chai *et al.* 2016, 2019), Rayleigh–Bénard convection (Pelusi *et al.* 2021), active fluid (Cates *et al.* 2008; Doostmohammadi *et al.* 2016; Carenza *et al.* 2019; Negro *et al.* 2019), isotropic turbulence (Perlekar *et al.* 2014; Milan *et al.* 2020), solid-liquid-vapor phase transition and phase ordering under various conditions (Osborn *et al.* 1995; Gonnella *et al.* 1997; Corberi *et al.* 1998; Kendon *et al.* 1999; Sofonea *et al.* 2004; Gonnella *et al.* 2010; Coclite *et al.* 2014; Wang *et al.* 2017; Ambrus *et al.* 2019; Busuioc *et al.* 2020; Huang *et al.* 2021b; Chen *et al.* 2021c).

Notwithstanding significant progress, the highly non-equilibrium interfacial thermohydrodynamics, which is strongly associated with the growth kinetics and morphological evolution of systems, is seldom reported and still poorly understood. This topic has presented a challenge to the important front of trans-scale modeling and simulation of multiphase flows.

Recently, we have demonstrated that the DBM offers a novel systematic scheme and a set of convenient and efficient tool for describing, measuring, and analyzing simultaneously THNE effects which cannot be adequately described by traditional hydrodynamic models (Xu *et al.* 2012; Gan *et al.* 2015; Lai *et al.* 2016; Gan *et al.* 2018; Zhang *et al.* 2019; Chen *et al.* 2020; Zhang *et al.* 2021; Chen *et al.* 2022a; Zhang *et al.* 2022a,b; Liu *et al.* 2022). DBM was developed from a branch of LBM which aims to describe the non-equilibrium flows from a more fundamental level and is no longer

based on the simple “propagation + collision” lattice gas evolution scenario. The key point of DBM is to ensure that the properties to be studied do not change with model simplification and use the non-conservative kinetic moments of  $(f - f^{(0)})$  to describe the system state and extract TNE and THNE information (Xu *et al.* 2018, 2021a,b,c), where  $f$  is the distribution function and  $f^{(0)}$  the equilibrium distribution function. Therefore, the simplified Boltzmann-like equation and kinetic moment relations which are not compliant with non-equilibrium statistical physics are prohibited in the DBM. Further, the DBM uses non-conservative kinetic moments of  $(f - f^{(0)})$  to open a phase space where the origin corresponds to the thermodynamic equilibrium state and other points correspond to specific THNE states. The phase space and its subspaces provide a graphic geometric description of non-equilibrium states. Evidently, each non-conservative kinetic moment of  $(f - f^{(0)})$  provides its specific contribution to the overall departure from local equilibrium. Hence, as explained above, the choice of the non-equilibrium moments to be retained is dictated by the specific problem at hand.

Methodologically, the DBM belongs to the general framework of non-equilibrium statistical physics, i.e. a specific form of coarse-graining as applied to the physics of fluids beyond the hydrodynamic level. Specifically, the THNE effects presented by the DBM have permitted to recover the main features of the distribution function (Lin *et al.* 2014; Su & Lin 2022), to capture various interfacial phenomena (Lin *et al.* 2014; Lai *et al.* 2016; Gan *et al.* 2019), to investigate entropy increasing mechanisms and their relative importance (Zhang *et al.* 2016, 2019), and to clarify some of the fundamental mechanisms of the fine structures of shock waves, contact discontinuities, rarefaction waves beyond the reach of molecular dynamics (Gan *et al.* 2018; Qiu *et al.* 2020, 2021; Bao *et al.* 2022). Kinetic features, such as the unbalancing and mutual conversion of internal energy at different degrees of freedom, provide appropriate criteria for determining whether or not higher-order TNE effects should be considered in the modeling and which level of DBM should be adopted (Lin *et al.* 2014; Gan *et al.* 2015, 2018). In plasma physics, kinetic features have been used to distinguish plasma shock wave from shock wave in ordinary neutral flow (Liu *et al.* 2022). These findings and observations shed light on the fundamental mechanisms of various compressible flow systems.

As for the more complicated multiphase case, in 2015, we proposed a DBM with a more realistic equation of state (EOS) to study the HNE and TNE manifestations induced by interparticle and gradient force during phase transition (Gan *et al.* 2015). We found that the maximum of TNE strength can be used as a physical criterion to discriminate the stages of spinodal decomposition and domain growth. In 2019, we further found that the maximum of entropy production rate can be used as another physical criterion to discriminate the two stages (Zhang *et al.* 2019). Whereas, these models are only suitable for cases with weak non-equilibrium effects, or cases in which the Knudsen number is sufficiently small, including phase separation with a slow quenching rate, shallow

quenching depth, limited liquid-vapor density ratio, weak viscous stress and heat flux, but wide interface width.

Two prominent reasons account for the insufficiency of the model far from equilibrium. First, constitutive relations are strictly associated with TNE measures, accounting for the coupling of distinct lengths or time scales, and ultimately determining the accuracy of the hydrodynamic model. Given that few kinetic moments are satisfied by the discrete equilibrium distribution function (DEDF), the model in the previous study (Gan *et al.* 2015) is only consistent with Onuki’s model (Onuki 2005, 2007) for Carnahan-Starling fluid in the hydrodynamic limit with linear constitutive relations, that is, Newton’s law of viscosity and Fourier’s law of heat conduction. Nevertheless, linear constitutive relations only result from the first-order deviation from the thermodynamic equilibrium, and are inadequate for cases with substantial HNE and TNE effects. Second, although higher-order TNE measures and their evolution can be extracted from this DBM (Gan *et al.* 2015), whether or not they are accurate enough should be carefully estimated, preserved, and improved.

In this study, we aim to develop a higher-order DBM for the multi-scale modeling of multiphase flow systems ranging from continuum to transition flow regimes. Following all the inspiring works on higher-order mesoscopic models for non-equilibrium ideal-gas flows (Shan *et al.* 2006; Zhang *et al.* 2006; Philippi *et al.* 2006; Li *et al.* 2019; Shi *et al.* 2021; Shi & Shan 2021; Meng *et al.* 2013; Ansumali *et al.* 2007; Chikatamarla & Karlin 2009; Montessori *et al.* 2015; Guo *et al.* 2015; Ambrus & Sofonea 2016; Coreixas *et al.* 2017; Yang *et al.* 2018; Xu *et al.* 2021*d*; Zhang *et al.* 2022*a*) is out of the scope of the present work, although they can be extended into multiphase flow systems with the approaches listed above. Instead, through Chapman-Enskog multi-scale expansion, we first establish the relationships between TNE measures and the generalized constitutive relations for viscous stress and heat flux beyond the Burnett level; formulate specific expressions with the second-order accuracy for viscous stress, heat flux, and other higher-order TNE and THNE quantities which are strictly associated with the evolution of constitutive relations. Moreover, we determine all the fewest required kinetic moments that the DEDF should satisfy, and construct three DBMs for multiphase flows near-equilibrium and far-from-equilibrium by inversely solving the required kinetic moments with efficient discrete-velocity models. Finally, we demonstrate theoretically and numerically that the capability of the DBM in describing TNE and THNE effects, as well as its multi-scale predictive capability, depend on the kinetic moments specifically recovered by the DEDF.

## 2. DBM for multiphase flows far-from-equilibrium

In this section, we first reconsider what the original Boltzmann Bhatnagar-Gross-Krook (BGK) model (Bhatnagar *et al.* 1954) describes and place the BGK model frequently

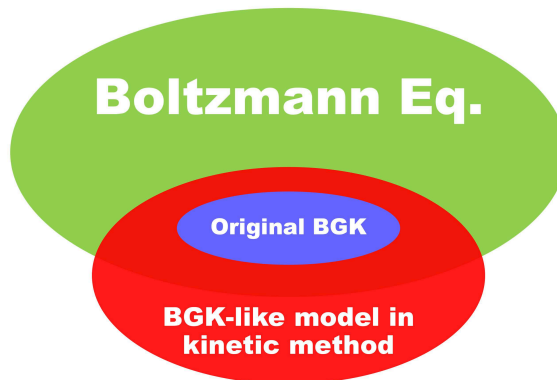


FIGURE 1. Schematic diagram of the application scopes of Boltzmann equation, the original BGK model and BGK-like model in kinetic method.

used for various non-equilibrium flows, in the proper theoretical perspective for the description of non-dilute systems. Then, we focus on the establishment of the links among Boltzmann-BGK equation, extended hydrodynamic models and THNE phenomena; we determine the necessary kinetic moments to measure THNE effects and discretize phase space using a moment-matching approach. Finally, we present the application of DBMs to multiphase flows far from equilibrium.

### 2.1. Discrete formulation of density functional kinetic theory

Extended hydrodynamics or generalized hydrodynamics models consider non-equilibrium effects through nonlinear constitutive relations. Correspondingly, high-order kinetic models consider non-equilibrium effects via higher-order distribution functions deviating from equilibrium. As a result, they are expected to be applicable to flows in the slip and transition flow regimes where the NS equations perform poorly (Struchtrup 2005; Gao & Sun 2014). A popular strategy for deriving such models is to perform a Chapman-Enskog (CE) multi-scale expansion. In a multiphase system, the starting point is the BGK Boltzmann equation, supplemented by an appropriate interparticle force (Gonnella *et al.* 2007)

$$\partial_t f + \mathbf{v} \cdot \nabla f = -\frac{1}{\tau}[f - f^{(0)}] + I, \quad (2.1)$$

where  $f^{(0)} = \frac{\rho}{2\pi T} \exp[-\frac{\mathbf{v}^* \cdot \mathbf{v}^*}{2T}]$  with  $\rho$ ,  $T$ ,  $\mathbf{v}^*$  are the local density, temperature, and thermal velocity, respectively. Here  $\mathbf{v}^* = \mathbf{v} - \mathbf{u}$ , with  $\mathbf{v}$  the particle velocity,  $\mathbf{u}$  the fluid velocity. Finally,  $I$  indicates the kinetic formulation of interparticle force accounting for the non-ideal gas effects.

At this stage, it is important to point out that the original BGK equation (Bhatnagar *et al.* 1954) assumes that the net effect of collisions is to relax the velocity distribution function towards a local equilibrium distribution  $f^{(0)}$ , over a microscopic velocity-independent characteristic timescale  $\tau$ . As a result, it describes molecular collisions in an averaged statistical form, with the only constraint of preserving mass-momentum-energy

conservation, as well as the  $H$ -theorem to secure convergent evolution towards a local equilibrium. Strictly speaking, the BGK model is valid only close to equilibrium, i.e.  $Kn \ll 1$  and  $f \simeq f^{(0)}$ , thus covering only a very small portion of the full kinetic space.

To study the kinetic behavior of non-ideal fluids far from equilibrium, one needs to account for interparticle interactions beyond binary collisions, as well as non-equilibrium effects triggered by strong inhomogeneities. This can be achieved by resorting to a mean-field theory formulation (Stanley 1971), or, more precisely, to a density functional kinetic theory (DFKT) (Succi *et al.* 2021). The role of DFKT is twofold: (1) Include the effects of the intermolecular interaction potential, omitted by the Boltzmann equation. (2) Extend the application scope of the BGK model to non-equilibrium phenomena beyond hydrodynamics. In a pictorial form (see figure 1), one could say that DFKT provides an “analytic continuation” of the BGK model to regions of kinetic phase space not covered by the original Boltzmann equation itself. Here, BGK-like refers to various families of model Boltzmann equations based on single and multi-time relaxation approximations.

In addition, the BGK-like models widely used in the study of complex fluids include several other physical modeling improvements. For example, relaxation times related to local macroscopic quantities (Li & Zhang 2004; Li *et al.* 2015) and collision frequency (Struchtrup 1997); pseudo-equilibrium distribution functions that contain non-equilibrium information (Holway Jr. 1966; Shakhov 1968; Gao & Sun 2014; Shan *et al.* 2006; Meng & Zhang 2011; Watari 2016); internal degrees of freedom (Rykov 1975) and even quantum vibrational energy (Wu *et al.* 2021a); appropriate kinetic boundary conditions (Wagner & Pagonabarraga 2002; Sbragaglia & Succi 2005; Toschi & Succi 2005; Sofonea & Sekerka 2005; Benzi *et al.* 2006; Chikatamarla *et al.* 2006; Chen *et al.* 2013). These improved models permit to capture a wider range of Knudsen numbers and a higher degree of non-equilibrium.

The multi-scale multiphase DFKT is expected to contribute to the area of materials science for energy-environment applications (Succi *et al.* 2020) and medical purposes. For instance, they may help to understand the non-equilibrium transport processes of multiphase flow in proton exchange membrane fuel cells for obtaining better performance, lower cost, emission, and noise (Chen *et al.* 2021a); to investigate the non-equilibrium nucleate boiling mechanism and design suitable surface structures for enhancing nucleate boiling heat transfer efficiency (Biferale *et al.* 2012; Li *et al.* 2018, 2020; Fei *et al.* 2020); to optimize heat source location (Dai *et al.* 2020) and improve the latent heat thermal energy storage rate (Ren 2019; Tian *et al.* 2022); to conduct mesoscale simulations of blood flow (Dupin *et al.* 2006; Yan *et al.* 2012) and generation, transmission, and diffusion of bioaerosols (He *et al.* 2022).

In the present paper, as a specific example of DFKT, the mean-field force  $I$  takes the following form for a liquid-vapor system

$$I = -[A + \mathbf{B} \cdot \mathbf{v}^* + (C + C_q)\mathbf{v}^* \cdot \mathbf{v}^*]f^{(0)}. \quad (2.2)$$



The coefficients in (2.2) are designed so as to recover the thermohydrodynamic equations proposed by Onuki (Onuki 2005) by using the following contributions of the force term  $I$  to mass, momentum, and energy equations at the second order in Knudsen number,

$$\int_{-\infty}^{\infty} I d\mathbf{v} = A + 2(C + C_q)T, \quad (2.3)$$

$$\int_{-\infty}^{\infty} I \mathbf{v} d\mathbf{v} = -\rho T \mathbf{B}, \quad (2.4)$$

$$\int_{-\infty}^{\infty} I \frac{\mathbf{v} \cdot \mathbf{v}}{2} d\mathbf{v} = -2\rho T^2(C + C_q) - \rho T \mathbf{B} \cdot \mathbf{u}. \quad (2.5)$$

As a result,  $A = -2(C + C_q)T$ , indicates that the forcing term guarantees mass conservation;  $\mathbf{B} = \frac{1}{\rho T}[\nabla(P^{\text{CS}} - \rho T) + \nabla \cdot \mathbf{A}]$ , describes two contributions of  $I$  to the fluid momentum. One comes from the difference between non-ideal gas EOS and ideal gas EOS, and the other from contribution of density gradient to pressure tensor  $\mathbf{A} = K \nabla \rho \nabla \rho - K(\rho \nabla^2 \rho + |\nabla \rho|^2 / 2) \mathbf{I} - [\rho T \nabla \rho \cdot \nabla(K/T)] \mathbf{I}$ , with  $\mathbf{I}$  the unit tensor,  $K$  the surface tension coefficient. Here we choose the Carnahan-Starling EOS (Carnahan & Starling 1969) as the non-ideal one  $P^{\text{CS}} = \rho T \frac{1+\eta+\eta^2-\eta^3}{(1-\eta)^3} - a\rho^2$  with  $\eta = b\rho/4$ , which offers a more accurate representation for hard sphere interactions than the van der Waals EOS. More realistic EOS, such as the Redlich-Kwong (Redlich & Kwong 1949), the Peng-Robinson EOS (Peng & Robinson 1976) could be conveniently incorporated into the DBM through modifying the extra force term  $I$  for modeling improvement.  $C = \frac{1}{2\rho T^2} \{ (P^{\text{CS}} - \rho T) \nabla \cdot \mathbf{u} + \mathbf{A} : \nabla \mathbf{u} + a\rho^2 \nabla \cdot \mathbf{u} + K[-\frac{1}{2}(\nabla \rho \cdot \nabla \rho) \nabla \cdot \mathbf{u} - \rho \nabla \rho \cdot \nabla(\nabla \cdot \mathbf{u}) - \nabla \rho \cdot \nabla \mathbf{u} \cdot \nabla \rho] \}$ , represents a partial contribution of  $I$  to energy. The term  $C_q = \frac{1}{2\rho T^2} \nabla \cdot [2q\rho T \nabla T]$ , permits to tune the heat conductivity independently of the dynamic viscosity (non-unit Prandtl number).

Constructing the density, momentum and energy kinetic moments of (2.1) and recomposing the time derivative, result in the following extended hydrodynamics equations:

$$\partial_t \rho + \nabla \cdot (\rho \mathbf{u}) = 0, \quad (2.6)$$

$$\partial_t (\rho \mathbf{u}) + \nabla \cdot (\rho \mathbf{u} \mathbf{u} + \mathbf{\Pi} + \mathbf{\Delta}_2) = 0, \quad (2.7)$$

$$\partial_t e_T + \nabla \cdot [e_T \mathbf{u} + \mathbf{\Pi} \cdot \mathbf{u} + \mathbf{\Delta}_{3,1} + \kappa_2 \nabla T] = 0, \quad (2.8)$$

where  $\mathbf{\Pi} = P^{\text{CS}} \mathbf{I} + \mathbf{A}$  is the nonviscous stress,  $e_T = \rho T - a\rho^2 + K|\nabla \rho|^2/2 + \rho u^2/2$  is the total energy density,  $\kappa_2 = 2\rho T q$  is an additional heat conductivity originated from  $C_q$  and designed to tune the Prandtl number.  $\mathbf{\Delta}_2$  and  $\mathbf{\Delta}_{3,1}$  are typical non-equilibrium measures related to the generalized constitutive relations.

Without loss of generality, two sets of non-equilibrium measures can be defined (Xu *et al.* 2012; Gan *et al.* 2015),

$$\mathbf{\Delta}_{m,n} = \mathbf{M}_{m,n}(f - f^{(0)}) = \int_{-\infty}^{\infty} \left(\frac{1}{2}\right)^{1-\delta_{m,n}} (f^{(1)} + f^{(2)} + \dots) \underbrace{\mathbf{v} \mathbf{v} \dots \mathbf{v}}_n (\mathbf{v} \cdot \mathbf{v})^{\frac{m-n}{2}} d\mathbf{v}, \quad (2.9)$$

$$\Delta_{m,n}^* = \mathbf{M}_{m,n}^*(f - f^{(0)}) = \int_{-\infty}^{\infty} \left(\frac{1}{2}\right)^{1-\delta_{m,n}} (f^{(1)} + f^{(2)} + \dots) \underbrace{\mathbf{v}^* \mathbf{v}^* \cdots \mathbf{v}^*}_{n} (\mathbf{v}^* \cdot \mathbf{v}^*)^{\frac{m-n}{2}} d\mathbf{v}, \quad (2.10)$$

where  $\Delta_{m,n}$  and  $\Delta_{m,n}^*$  are the  $m$ -th order tensors contracted to  $n$ -th order ones, and  $\delta_{m,n}$  is the Kronecker delta function. Here  $(m-n)/2$  is an integer, when  $m=n$ ,  $\Delta_{m,n}$  and  $\Delta_{m,n}^*$  are simplistically referred to as  $\Delta_m$  and  $\Delta_m^*$ , respectively. Here  $\Delta_{m,n}$  describes the combination effects of HNE and TNE, which are usually called the thermo-hydrodynamic non-equilibrium (THNE) effects,  $\Delta_{m,n}^*$  reflects molecular individualism on top of organized collective motion, describing only the TNE effects;  $\Delta_{m,n} - \Delta_{m,n}^*$  depicts the HNE effects, as a supplemental description of macroscopic quantity gradients.  $\mathbf{M}_{m,n}$  ( $\mathbf{M}_{m,n}^*$ ) is the non-central (central) kinetic moment,  $f^{(j)}$  represents the  $j$ -th order derivation from  $f^{(0)}$ . The decomposition relations among THNE and TNE measures are derived and displayed in Appendix A,

$$\begin{aligned} \Delta_2 &= \Delta_2^*, \\ \Delta_{3,1} &= \Delta_{3,1}^* + \Delta_2^* \cdot \mathbf{u}, \\ \Delta_3 &= \Delta_3^* + (u_\alpha \Delta_{2\beta\gamma}^* + u_\beta \Delta_{2\alpha\gamma}^* + u_\gamma \Delta_{2\alpha\beta}^*) \mathbf{e}_\alpha \mathbf{e}_\beta \mathbf{e}_\gamma, \\ \Delta_{4,2} &= \Delta_{4,2}^* + \Delta_{3,1}^* \mathbf{u} + \mathbf{u} \Delta_{3,1}^* + \Delta_3^* \cdot \mathbf{u} + \Delta_2^* \cdot \mathbf{u} \mathbf{u} + \mathbf{u} \Delta_2^* \cdot \mathbf{u} + \frac{u^2}{2} \Delta_2^*. \end{aligned} \quad (2.11)$$

Here  $\Delta_2^*$  and  $\Delta_{3,1}^*$  are also referred to as the non-organized moment flux (NOMF) and non-organized energy flux (NOEF), respectively. Compared with the NS and Burnett equations,  $\Delta_2^*$  and  $\Delta_{3,1}^*$  correspond to more generalized viscous stress and heat flux, which contain all hierarchical TNE effects induced by  $(f - f^{(0)})$ , instead of only  $f^{(1)}$  at the NS level and  $f^{(1)} + f^{(2)}$  at the Burnett level. The links among BE, the extended hydrodynamic equations, and TNE measures have been established so far.  $\Delta_3^*$  and  $\Delta_{4,2}^*$  are flux of viscous stress and flux of heat flux, respectively.

However,  $\Delta_2^*$  and  $\Delta_{3,1}^*$  are primarily unknown. To obtain the explicit constitutive relations, we perform Chapman-Enskog expansion on both sides of (2.1) by introducing expansions

$$f = f^{(0)} + f^{(1)} + f^{(2)} + \dots, \quad (2.12)$$

$$\partial_t = \partial_{t_1} + \partial_{t_2} + \dots, \quad (2.13)$$

$$\nabla = \nabla_1, \quad I = I_1, \quad (2.14)$$

where  $\partial_{t_j}$ ,  $\nabla_j$ , and  $I_j$  are  $j$ -th order terms in Knudsen number  $\epsilon$ . Substituting equations (2.12)-(2.14) into (2.1) and equating terms that have the same orders in  $\epsilon$  give

$$\epsilon^1 : \partial_{t_1} f^{(0)} + \nabla_1 \cdot (f^{(0)} \mathbf{v}) = -\frac{1}{\tau} f^{(1)} + I_1, \quad (2.15)$$

$$\epsilon^2 : \partial_{t_2} f^{(0)} + \partial_{t_1} f^{(1)} + \nabla_1 \cdot (f^{(1)} \mathbf{v}) = -\frac{1}{\tau} f^{(2)}. \quad (2.16)$$

Performing the velocity moments with the collision invariant vector  $(1, \mathbf{v}, \frac{v^2}{2})$  on the two sides of (2.15), leads to the useful relations between the temporal derivative  $\partial_{t_1}$  and the

spatial derivative  $\nabla_1$  at  $\epsilon^1$  level

$$\partial_{t_1}\rho = -\nabla_1 \cdot (\rho \mathbf{u}), \quad (2.17)$$

$$\partial_{t_1}\mathbf{u} = -T\mathbf{B} - \nabla_1 T - \frac{T}{\rho}\nabla_1\rho - \mathbf{u} \cdot \nabla_1\mathbf{u}, \quad (2.18)$$

$$\partial_{t_1}T = -2(C + C_q)T^2 - T\nabla_1 \cdot \mathbf{u} - \mathbf{u} \cdot \nabla_1 T. \quad (2.19)$$

From (2.15), we can obtain  $f^{(1)} = -\tau[\partial_{t_1}f^{(0)} + \nabla_1 \cdot (f^{(0)}\mathbf{v}) - I_1]$ . Using (2.17)-(2.19) and after some straightforward but rather tedious algebraic manipulation, we acquire the following relations between thermodynamic forces and fluxes

$$\Delta_2^{*(1)} = \int_{-\infty}^{\infty} f^{(1)}\mathbf{v}^*\mathbf{v}^* d\mathbf{v} = -\mu[\nabla\mathbf{u} + (\nabla\mathbf{u})^T - \mathbf{I}\nabla \cdot \mathbf{u}], \quad (2.20)$$

$$\Delta_{3,1}^{*(1)} = \int_{-\infty}^{\infty} \frac{1}{2}f^{(1)}\mathbf{v}^* \cdot \mathbf{v}^*\mathbf{v}^* d\mathbf{v} = -\kappa_1\nabla T, \quad (2.21)$$

Equations (2.20)-(2.21) indicate that the first-orders of NOMF and NOEF are exactly the viscous stress tensor and the heat flux at the NS level, respectively;  $\mu = \rho T\tau$  is the viscosity coefficient and  $\kappa_1 = 2\rho T\tau$  the heat conductivity. Similarly, we have

$$\Delta_3^{*(1)} = \int_{-\infty}^{\infty} f^{(1)}\mathbf{v}^*\mathbf{v}^*\mathbf{v}^* d\mathbf{v} = -\rho T\tau(\partial_\alpha T\delta_{\beta\gamma} + \partial_\beta T\delta_{\alpha\gamma} + \partial_\gamma T\delta_{\alpha\beta})\mathbf{e}_\alpha\mathbf{e}_\beta\mathbf{e}_\gamma. \quad (2.22)$$

$$\Delta_{4,2}^{*(1)} = \int_{-\infty}^{\infty} f^{(1)}\mathbf{v}^*\mathbf{v}^*\frac{\mathbf{v}^* \cdot \mathbf{v}^*}{2}d\mathbf{v} = -3\rho T^2\tau[\nabla\mathbf{u} + (\nabla\mathbf{u})^T - \mathbf{I}\nabla \cdot \mathbf{u}]. \quad (2.23)$$

Deeper TNE effects can be accessed by considering the contributions of  $f^{(2)}$ , and clarifying relations between  $\partial_{t_2}$  and  $\nabla_1$  at  $\epsilon^2$  level according to similar procedures listed in (2.17)-(2.19). Specifically, from (2.16), we acquire

$$\begin{aligned} f^{(2)} &= -\tau[\partial_{t_2}f^{(0)} + \partial_{t_1}f^{(1)} + \nabla_1 \cdot (f^{(1)}\mathbf{v})] \\ &= -\tau\partial_{t_2}f^{(0)} + \tau^2\partial_{t_1}^2f^{(0)} + \tau^2\partial_{t_1}[\nabla_1 \cdot (f^{(0)}\mathbf{v})] - \tau^2\partial_{t_1}I_1 \\ &\quad + \tau^2\nabla_1 \cdot [\partial_{t_1}f^{(0)}\mathbf{v} + \nabla_1 \cdot (f^{(0)}\mathbf{v}\mathbf{v}) - I_1\mathbf{v}]. \end{aligned} \quad (2.24)$$

It is clear that  $f^{(2)}$  can also be expressed in terms of  $f^{(0)}$ . As a result, non-conservative non-equilibrium moments, can finally resort to those of  $f^{(0)}$ , which triggers the requirement of the more higher-order kinetic moments of  $f^{(0)}$ . The second order non-organized moment flux reads

$$\Delta_2^{*(2)} = \mathbf{M}_2^*(f^{(2)}) = \int_{-\infty}^{\infty} f^{(2)}\mathbf{v}^*\mathbf{v}^* d\mathbf{v}. \quad (2.25)$$

To obtain an explicit expression, relations between  $\partial_{t_2}$  and  $\nabla_1$  at  $\epsilon^2$  level should be clarified. Performing the velocity moments with the collision invariant vector  $(1, \mathbf{v}, \frac{v^2}{2})$  on the two sides of equation (2.16), leads to the useful relations between the temporal derivative  $\partial_{t_2}$  and the spatial derivative  $\nabla_1$  at  $\epsilon^2$  level

$$\partial_{t_2}\rho = 0, \quad (2.26)$$

$$\rho\partial_{t_2}\mathbf{u} = -\nabla_1 \cdot \Delta_2^{*(1)}, \quad (2.27)$$

$$\partial_{t_2}(\rho T + \frac{1}{2}\rho u^2) = -\nabla_1 \cdot \Delta_{3,1}^{(1)}. \quad (2.28)$$

Using Eqs. (2.26)-(2.28) to replace the temporal derivative  $\partial_{t_2}$  by spatial derivative  $\nabla_1$  at  $\epsilon^2$  level, and after some laborious algebraic manipulation, we acquire expression for  $\Delta_2^{*(2)}$ . Likewise, analytical expressions for  $\Delta_{3,1}^{*(2)}$ ,  $\Delta_3^{*(2)}$  and  $\Delta_{4,2}^{*(2)}$  can be obtained, as illustrated in Appendix B. The derivation of these expressions is a tough task, so we resort to software, Maple 18.

Furthermore, multiplying (2.1) by  $\mathbf{v}^* \mathbf{v}^*$  and  $\frac{1}{2} \mathbf{v}^* \cdot \mathbf{v}^* \mathbf{v}^*$ , and integrating over the whole velocity space, we obtain the time evolution equations for viscous stress and heat flux,

$$\partial_t \Delta_2^* + \partial_t \mathbf{M}_2^*(f^{(0)}) + \nabla \cdot [\mathbf{M}_3^*(f^{(0)}) + \mathbf{M}_2^*(f^{(0)}) \mathbf{u} + \Delta_3^* + \Delta_2^* \mathbf{u}] = -\frac{1}{\tau} \Delta_2^* + \mathbf{M}_2^*(I), \quad (2.29)$$

$$\partial_t \Delta_{3,1}^* + \partial_t \mathbf{M}_{3,1}^*(f^{(0)}) + \nabla \cdot [\mathbf{M}_{4,2}^*(f^{(0)}) + \mathbf{M}_{3,1}^*(f^{(0)}) \mathbf{u} + \Delta_{4,2}^* + \Delta_{3,1}^* \mathbf{u}] = -\frac{1}{\tau} \Delta_{3,1}^* + \mathbf{M}_{3,1}^*(I). \quad (2.30)$$

Equations (2.29) and (2.30) suggest that obtaining the expressions of higher-order TNE quantities, such as  $\Delta_3^*$  and  $\Delta_{4,2}^*$ , enhances our understanding of the evolution mechanisms of nonlinear constitutive relations.

To summarize, higher-order constitutive relations of second-order accuracy for viscous stress and heat transfer can be formulated as  $\Delta_2^* = \Delta_2^{*(1)} + \Delta_2^{*(2)}$ ,  $\Delta_{3,1}^* = \Delta_{3,1}^{*(1)} + \Delta_{3,1}^{*(2)}$ , which are expected to noticeably improve the macroscopic modeling. Meanwhile, higher-order TNE measures with second-order accuracy,  $\Delta_3^* = \Delta_3^{*(1)} + \Delta_3^{*(2)}$ ,  $\Delta_{4,2}^* = \Delta_{4,2}^{*(1)} + \Delta_{4,2}^{*(2)}$ , offer more abundant non-equilibrium scenarios from different aspects and are useful in elucidating the evolutions of higher-order constitutive relations.

In fact, the theoretical expressions of  $\Delta_3^*$  and  $\Delta_{4,2}^*$  are also constitutive relations, which are omitted in the NS equations. In the case of quasi-continuous and near-equilibrium, it is not a big problem if they are omitted. However, as the degree of discretization and thermodynamic non-equilibrium increase, ignoring  $\Delta_3^*$  and  $\Delta_{4,2}^*$  leads to substantial errors. Furthermore, the analytical expressions for THNE with second-order accuracy,  $\Delta_2 = \Delta_2^{(1)} + \Delta_2^{(2)}$ ,  $\Delta_{3,1} = \Delta_{3,1}^{(1)} + \Delta_{3,1}^{(2)}$ ,  $\Delta_3 = \Delta_{3,1}^{(1)} + \Delta_{3,1}^{(2)}$ , and  $\Delta_{4,2} = \Delta_{4,2}^{(1)} + \Delta_{4,2}^{(2)}$  can be acquired from (2.11).

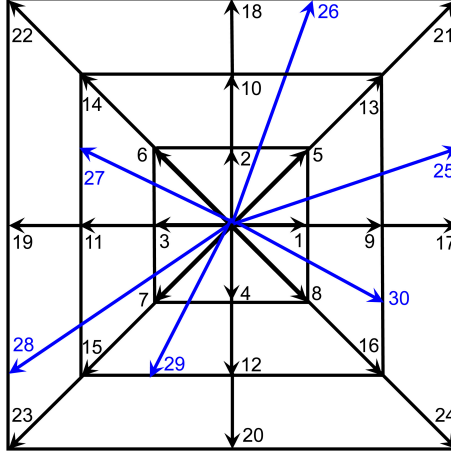
## 2.2. Discretization of particle velocity space

The velocity space discretization is a critical step in DBM modeling. The above expressions for TNE measures (see Appendix B) have been derived from the (2.1) with a continuous equilibrium distribution function  $f^{(0)}$ . To conduct numerical simulation, it is required to construct a discrete-velocity model (DVM)  $\mathbf{v}_i$  to discretize the particle velocity space, and formulate the DEDF  $f_i^{(0)}$  satisfying all the needed kinetic moments, where  $i = 1, 2, 3, \dots, N$ , with  $N$  the total number of discrete velocities. Chapman-Enskog analysis demonstrates that  $f_i^{(0)}$  should satisfy the following seven kinetic moments (Gan *et al.* 2015):  $\mathbf{M}_0$ ,  $\mathbf{M}_1$ ,  $\mathbf{M}_{2,0}$ ,  $\mathbf{M}_2$ ,  $\mathbf{M}_{3,1}$ ,  $\mathbf{M}_3$ ,  $\mathbf{M}_{4,2}$  in the recovery of the targeted hydrodynamic equations at the NS level. In cases with fixed specific heat-ratio,  $\mathbf{M}_0$ ,  $\mathbf{M}_1$ ,  $\mathbf{M}_2$ ,  $\mathbf{M}_3$ ,  $\mathbf{M}_{4,2}$

TNE Required higher-order kinetic moments

$\Delta_3^{*(1)}$	$\mathbf{M}_4$	$\mathbf{M}_5$		
$\Delta_{3,1}^{*(1)}$	$\mathbf{M}_{5,1}$			
$\Delta_{4,2}^{(1)}$	$\mathbf{M}_{5,3}$	$\mathbf{M}_{6,2}$		
$\Delta_2^{*(2)}$	$\mathbf{M}_4$	$\mathbf{M}_{5,3}$		
$\Delta_3^{*(2)}$	$\mathbf{M}_4$	$\mathbf{M}_5$	$\mathbf{M}_{5,3}$	$\mathbf{M}_{6,4}$
$\Delta_{3,1}^{*(2)}$	$\mathbf{M}_{5,1}$	$\mathbf{M}_{5,3}$	$\mathbf{M}_{6,2}$	
$\Delta_{4,2}^{*(2)}$	$\mathbf{M}_{5,3}$	$\mathbf{M}_{6,2}$	$\mathbf{M}_{6,4}$	$\mathbf{M}_{7,3}$

TABLE 1. Higher-order kinetic moment relations required for deriving the analytical expressions of TNE measures, where the blue ones are independent constraint relations.

FIGURE 2. Schematic of the D2V30 discrete-velocity model, where  $\mathbf{v}_1, \mathbf{v}_2, \dots, \mathbf{v}_{24}$  are symmetric vectors, and  $\mathbf{v}_{25}, \mathbf{v}_{26}, \dots, \mathbf{v}_{30}$  are non-symmetric ones, designed to guarantee the existence of  $\Psi^{-1}$ .

are independent. In the recovery of the targeted hydrodynamic equations at the Burnett level,  $f_i^{(0)}$  should further satisfy  $\mathbf{M}_4$  and  $\mathbf{M}_{5,3}$  (Gan *et al.* 2018). In the recovery of the targeted hydrodynamic equations beyond the Burnett level and description of all the TNE measures displayed in Appendix B with second-order accuracy,  $f_i^{(0)}$  should satisfy more higher-order non-equilibrium moments, as listed in Table 1. Among them,  $\mathbf{M}_0, \mathbf{M}_1, \mathbf{M}_2, \mathbf{M}_3, \mathbf{M}_4, \mathbf{M}_5, \mathbf{M}_{6,4}$ , and  $\mathbf{M}_{7,3}$  are independent (see Appendix C).

Here, “satisfy” means that the required kinetic moments of  $f_i^{(0)}$ , originally in integral form, can be calculated in discrete summation form

$$\Phi_n(f^{(0)}) = \int_{-\infty}^{\infty} f^{(0)} \Psi d\mathbf{v} = \sum_i f_i^{(0)} \Psi_i, \quad (2.31)$$

with  $\Psi = [1, \mathbf{v}, \mathbf{v}\mathbf{v}, \mathbf{v}\mathbf{v}\mathbf{v}, \mathbf{v}\mathbf{v}\mathbf{v}\mathbf{v}, \mathbf{v}\mathbf{v}\mathbf{v}\mathbf{v}\mathbf{v}, \frac{1}{2}\mathbf{v} \cdot \mathbf{v}\mathbf{v}\mathbf{v}\mathbf{v}\mathbf{v}, \frac{1}{2}(\mathbf{v} \cdot \mathbf{v})^2 \mathbf{v}\mathbf{v}\mathbf{v}]^T$ . Equation (2.31) can

---

DVMs	Satisfied independent kinetic moments
D2V13	$\mathbf{M}_0, \mathbf{M}_1, \mathbf{M}_2, \mathbf{M}_3, \mathbf{M}_{4,2}$
D2V15	$\mathbf{M}_0, \mathbf{M}_1, \mathbf{M}_2, \mathbf{M}_3, \mathbf{M}_{4,2}, \mathbf{M}_{5,1}$
D2V16	$\mathbf{M}_0, \mathbf{M}_1, \mathbf{M}_{2,0}, \mathbf{M}_2, \mathbf{M}_{3,1}, \mathbf{M}_3, \mathbf{M}_{4,2}$
D2V30	$\mathbf{M}_0, \mathbf{M}_1, \mathbf{M}_2, \mathbf{M}_3, \mathbf{M}_4, \mathbf{M}_5, \mathbf{M}_{6,4}, \mathbf{M}_{7,3}$

---

TABLE 2. Discrete-velocity models and corresponding independent kinetic moments.

be rewritten in a matrix form

$$\Phi_n = \Psi \cdot \mathbf{f}^{(0)}, \quad (2.32)$$

where  $\Phi_n = (\mathbf{M}_0, \mathbf{M}_1, \mathbf{M}_2, \mathbf{M}_3, \mathbf{M}_4, \mathbf{M}_5, \mathbf{M}_{6,4}, \mathbf{M}_{7,3})^T = (M_0, M_{1x}, M_{1y}, \dots, M_{7,3yyy})^T$  is the set of moments of  $f^{(0)}$ .  $\mathbf{f}^{(0)} = (f_1^{(0)}, f_2^{(0)}, \dots, f_{30}^{(0)})^T$ ,  $\Psi = (\mathbf{C}_1, \mathbf{C}_2, \dots, \mathbf{C}_{30})$  is a  $30 \times 30$  matrix bridging the DEDF and the kinetic moments with  $\mathbf{C}_i = (1, v_{ix}, v_{iy}, \dots, \frac{1}{2}v^4 v_{ix}^3, \frac{1}{2}v^4 v_{ix}^2 v_{iy}, \frac{1}{2}v^4 v_{ix} v_{iy}^2, \frac{1}{2}v^4 v_{iy}^3)^T$ . Naturally,  $\mathbf{f}^{(0)}$  can be calculated as follows (Gan *et al.* 2013),

$$\mathbf{f}^{(0)} = \Psi^{-1} \cdot \Phi_n, \quad (2.33)$$

where  $\Psi^{-1}$  is the inverse matrix of  $\Psi$ . Here, a two-dimensional DVM with 30 discrete velocities, schematically drawn in figure 2, is used to discretize the velocity space and to ensure the existence of  $\Psi^{-1}$

$$(v_{ix}, v_{iy}) = \begin{cases} \text{cyc} : c(\pm 1, 0) & \text{for } 1 \leq i \leq 4 \\ c(\pm 1, \pm 1) & \text{for } 5 \leq i \leq 8 \\ \text{cyc} : 2c(\pm 1, 0) & \text{for } 9 \leq i \leq 12 \\ 2c(\pm 1, \pm 1) & \text{for } 13 \leq i \leq 16 \\ \text{cyc} : 3c(\pm 1, 0) & \text{for } 17 \leq i \leq 20 \\ 3c(\pm 1, \pm 1) & \text{for } 21 \leq i \leq 24 \\ c(3, 1), c(1, 3) & \text{for } i = 25, 26 \\ c(-2, 1), c(-3, -2) & \text{for } i = 27, 28 \\ c(-1, -2), c(2, -1) & \text{for } i = 29, 30 \end{cases}, \quad (2.34)$$

where ‘‘cyc’’ indicates cyclic permutation. The selection of  $\mathbf{v}_{25}, \dots, \mathbf{v}_{30}$  is highly flexible and thus guarantees the existence of  $\Psi^{-1}$  and optimizes the stability of the model. Then the discrete coarse-grained evolution equation reads

$$\partial_t f_i + \mathbf{v}_i \cdot \nabla f_i = -\frac{1}{\tau} [f_i - f_i^{(0)}] + I_i. \quad (2.35)$$

It is necessary to point out that:

(i) The most important step in DBM modeling and simulation is the calculation of  $f_i^{(0)}$ . The Maxwell distribution satisfies an infinite number of moment relations. Requiring  $f_i^{(0)}$  to satisfy all the moment relations is impractical. Which moment relations are necessary depends on the kinetic properties to be studied, a choice that is typically dictated by the intensity of the non-equilibrium effects to be described.

(ii) The capability of describing non-equilibrium effects relies on the kinetic moment relations that the DBM correctly retrieved. Therefore, by satisfying different kinetic moments, we can systematically construct DBMs for TNE effects at various levels that correspond to different coarse-grained models and own different application ranges. For instance, besides the D2V30 DBM, we propose D2V13, D2V15, and D2V16 multiphase models, and examine their performances in the subsequent section. Here, the D2V13 (D2V15) model adopts the former 13 (15) discrete velocities of the D2V30 model. D2V16 model indicates the one proposed in (Gan *et al.* 2013) for compressible flows with a flexible specific heat ratio. While considering only the translational degrees of freedom, the D2V16 model will degenerate into the D2V13 model. Independent kinetic moments retrieved by these models are exhibited in Table 2.

(iii) For the same set of grids, the computational cost of the model is proportional to the number of discrete velocities. So, theoretically, the computational cost of the D2V30 model is twice that of the D2V15 model. Compared with the standard multiphase lattice Boltzmann model, such as the well-known Shan-Chen D2Q9 model (Wang *et al.* 2009), the computational cost of D2V30 model is about 4.4 times that of the D2Q9 model, greater than the ratio of the number of discrete velocities of the two DVMS 30/9. This origins from the more concise external force term of the Shan-Chen model.

(iv) The complexity of corresponding hydrodynamic equations increases sharply with the degree of TNE, whereas that of the DBM does not have a significant increase. We can formulate DBM with the desired order of accuracy by incorporating more needed kinetic moments into  $\Phi_n$ , and perform simulations without knowing the exact form of the hydrodynamic equations. For example, the D2V30 model satisfies 8 moment relations listed in Table 2 and describes viscous stress and heat flux with third-order accuracy. If one wants to achieve fourth-order accuracy, the physical model needs to further satisfy higher-order moment relations  $\mathbf{M}_6$  and  $\mathbf{M}_{7.5}$ . Then the independent ones are  $\mathbf{M}_0$ ,  $\mathbf{M}_1$ ,  $\mathbf{M}_2$ ,  $\mathbf{M}_3$ ,  $\mathbf{M}_4$ ,  $\mathbf{M}_5$ ,  $\mathbf{M}_6$  and  $\mathbf{M}_{7.5}$ . For a two-dimensional case, these moment relations have 34 independent components, so a D2V34 model is sufficient to discretize the phase space. Compared with the D2V30 model, the computational cost of the D2V34 model is only increased by 13.33%.

(v) The Chapman-Enskog expansion acts as a bridge between the kinetic description given by the DBM and continuum mechanics non-conserved macroscopic dissipation and the conserved variables. Through it, we can directly and strictly determine the minimal physical requirements, and confirm the invariable moment sets  $\Phi_n$  for modeling a given non-equilibrium state. We also point out that, from the perspective of perturbation theory, conducting Chapman-Enskog multi-scale analysis corresponds to imposing disturbance on the equilibrium system. The convergence of Chapman-Enskog multi-scale expansion corresponds to the system returning to its equilibrium state. If the disturbance is too strong, such as due to the emergence of very steep gradients, leading to the divergence of the Taylor expansion of the distribution function, then the

disturbance may trigger new structures or modes, and the Chapman-Enskog analysis fails. Fortunately, in the multiphase flow system, due to the existence of the interface with a certain width, the gradient of the macroscopic quantity is more gentle than that in the high-speed compressible single-phase system, especially in the low-speed multiphase flow with large surface tension.

(vi) Strictly speaking, the discretization of continuous space inevitably brings non-physical symmetry breaking, and is a source of physical and numerical inaccuracies in the description of the system. Coarse-grained physical modeling is inherently a trade-off. The properties to be studied must be preserved, beyond scope of the given study can be sacrificed. Of the many options available to meet the research needs of the current problem, the simplest or most economical is often the first choice. The moment matching approach, shown in (2.31), affords the minimal discrete velocity sets for solving  $\Phi_n$ , because the number of discrete velocities just equals the number of the independent kinetic moment relations. Therefore, physically, DBM proposed in this way features the highest computational efficiency. These outstanding advantages make DBM a particularly appealing methodology for investigating non-equilibrium flows. We can also build a more symmetrical DVM by increasing the number of discrete velocities. For example, we can construct a DVM through Hermite expansion (Shan *et al.* 2006; Zhang *et al.* 2006; Li *et al.* 2019; Shi *et al.* 2021; Gan *et al.* 2008) so that the DVM has better spatial symmetry at the cost of increasing the number of discrete velocities. In this paper, we have chosen the simplest form matching the relevant physical constraints for the problems at hand.

(vii) For bulk flow far from the boundary, DBM includes three main pillars described in the Abstract. For near-wall flow, the mechanism for THNE may be greatly different from that for bulk flow, and consequently, a fourth pillar, construction of kinetic boundary conditions, is necessary. A DBM for slip flow is referred to Zhang *et al.* (2022b).

(viii) The present work belongs to the category of single-component miscible multiphase flow. We have several works on DBM modeling and simulation of multi-component miscible fluid flows (Lin *et al.* 2016, 2017; Zhang *et al.* 2020; Lin *et al.* 2021). The extension of the present work to a multi-component immiscible fluid system is currently under consideration. For multi-component immiscible fluid flows, self-aggregation still occurs between different phases, and surface tension still exists between different components. The core of DBM modeling for immiscible multiphase flow is the incorporation of (a) intermolecular interaction in the same component and (b) intermolecular interaction between different components.

### 3. Numerical Simulations and Analysis

In this section, we first validate DBMs at various levels via three benchmarks related to the equilibrium properties in bulk regions; then evaluate carefully the multi-scale



predictive capability of the DBMs by investigating THNE features around the liquid-vapor interface; finally, study the effects of relaxation time and surface tension coefficient on thermal phase separation from the non-equilibrium aspects. In all simulations, we set  $a = 2$  and  $b = 0.4$ , then the critical density and temperature are  $\rho^c = 1.30444$  and  $T^c = 1.88657$ , respectively. To improve the numerical stability and accuracy, the windowed fast Fourier transform (FFT) scheme with 16-th order in precision (Gan *et al.* 2011, 2012b, 2015) is utilized to discretize the spatial derivatives, and the second-order Runge-Kutta scheme is used to calculate the temporal derivative. Notably, the periodic boundary condition is inherently imposed in the  $x$  and  $y$  directions because of the adoption of the FFT scheme. For a system with non-periodic boundary conditions, the FFT scheme can also be applied as long as the mirror operation is performed on the non-periodic boundary (Gan *et al.* 2012a), at the cost of doubling the calculation amount. All the parameters used here are dimensionless. Please refer to Zhang *et al.* (2019) for recovery of the actual physical quantities from the numerical results.

### 3.1. Verification and validation

#### 3.1.1. Liquid-vapor coexistence curve

Here the liquid-vapor coexistence curve test is used to check if the newly constructed DBMs can reproduce the correct equilibrium thermodynamics of the Carnahan-Starling system. For this problem considered, the initial conditions are  $(\rho, T, u_x, u_y) = (\rho_l, 1.82, 0.0, 0.0)$ , if  $N_x/4 < x \leq 3N_x/4$ ; else  $(\rho, T, u_x, u_y) = (\rho_v, 1.82, 0.0, 0.0)$ , where  $\rho_l = 1.9643$  and  $\rho_v = 0.7569$  are the theoretical liquid and vapor coexisting densities at  $T = 1.82$ . Parameters are as follows  $\tau = 10^{-4}$ ,  $K = 1.5 \times 10^{-4}$ ,  $\text{Pr} = 0.01$ ,  $N_x \times N_y = 128 \times 1$ ,  $c = 1.25$ ,  $\Delta t = 3 \times 10^{-5}$ ,  $\Delta x = \Delta y = 4 \times 10^{-3}$  for D2V13, D2V15 and D2V30 models. But in the D2V16 model, the minimum spatial step that stabilizes the simulation is  $\Delta x = \Delta y = 5 \times 10^{-3}$ . The initial temperature drops by 0.01 when a steady state has been reached, i.e.,  $|(u_x^2 + u_y^2)^{1/2}|_{\max} < 10^{-6}$ . Figure 3 displays the phase diagrams calculated from the DBM simulations and Maxwell construction. In each panel, the two sets of results are in good agreement with each other. However, the maximum density ratio  $R_{\max} = \rho_{\max}/\rho_{\min}$  and the lowest reduced temperature  $Tr_{\min} = T_{\min}/T^C$  that each model can undergo are quite different.

The more the moment relations maintained by the DBM, the larger the maximum density ratio and the lower the minimum reduced temperature that the model can attain. Specifically, in the D2V13 model,  $R_{\max} = 278.9$  with the maximum relative error in density  $\epsilon = |\rho_{\text{DBM}} - \rho_{\text{Exact}}|/\rho_{\text{Exact}} = 0.48\%$  in the vapor branch ( $\epsilon_{\max} = 0.28\%$  for the D2V30 model under the same density ratio). Whereas in the D2V30 model,  $R_{\max}$  can reach up to 404.1 and  $Tr_{\min}$  reduces to 0.53 with  $\epsilon = 1.12\%$  in the vapor branch.

There are several reasons that account for the fact that the incorporation of higher-order kinetic moments improves the density ratio that the model can sustain. Physically, the incorporation of higher-order moment relation makes the DBM model more

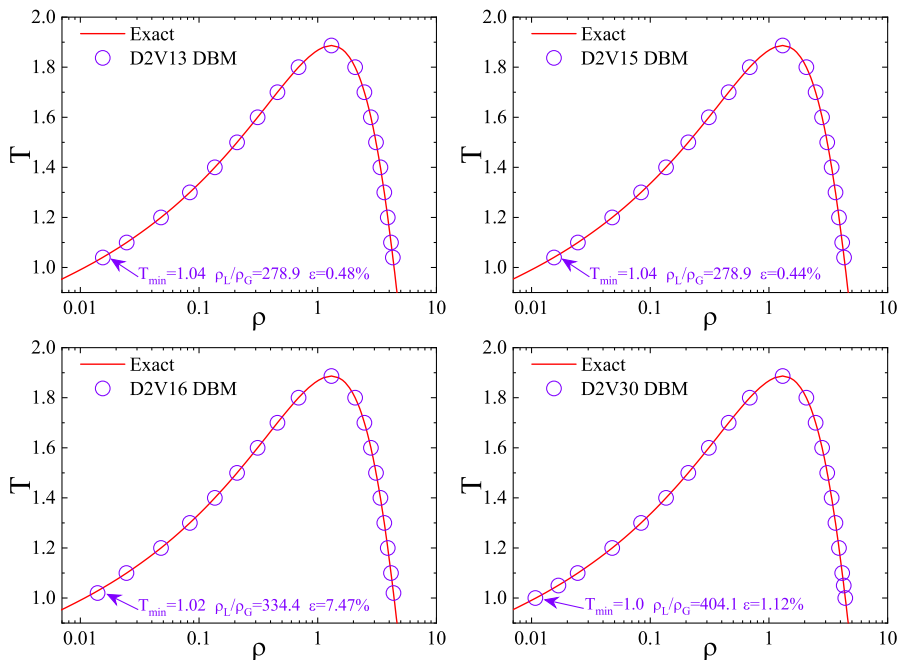


FIGURE 3. Comparisons of the coexisting densities predicted by various DBMs and Maxwell construction.

approximate to the continuous Boltzmann-BGK equation with an external force term, that is, the model is more physical; secondly, the incorporation of higher-order moment relation makes DBM more accurate in describing non-equilibrium effects, which greatly affects the computational accuracy and stability, as shown in figure 11; thirdly, the higher-order model is more capable of ensuring the positive entropy increase rate during the evolution process, with the entropy growth rate defined as (Zhang *et al.* 2019)  $\frac{dS}{dt} = \int (\Delta_{3,1}^* \cdot \nabla \frac{1}{T} - \frac{1}{T} \Delta_2^* : \nabla \mathbf{u}) d\mathbf{r}$ ; fourth, the incorporation of higher-order moment relation is equivalent to adopting more discrete velocities to discretize the phase space. As the number of discrete velocity increases, the fluctuation of distribution function  $\delta f$  and the spatial gradient of distribution function  $\nabla f$  decrease, which makes the higher-order model more stable. Lots of numerical examples suggest that the stability improvement of higher-order model compared to lower-order ones is effective not only for static (or quasi-static) tests, but also for dynamic cases.

### 3.1.2. Spurious velocity

Figure 4 illustrates the time evolutions of the maximum velocity  $u_{\max}$  for an initially non-equilibrium planar interface, obtained from various DBM simulations performed using the procedure and parameters exhibited in figure 3, except for the initial temperature is suddenly quenched from 1.45 to 1.10, and the relaxation time  $\tau = 2 \times 10^{-4}$ . The spurious velocity, mainly located around the liquid-vapor interface, refers to the residual velocity which cannot be further reduced after a long period of evolution (Wagner 2003).

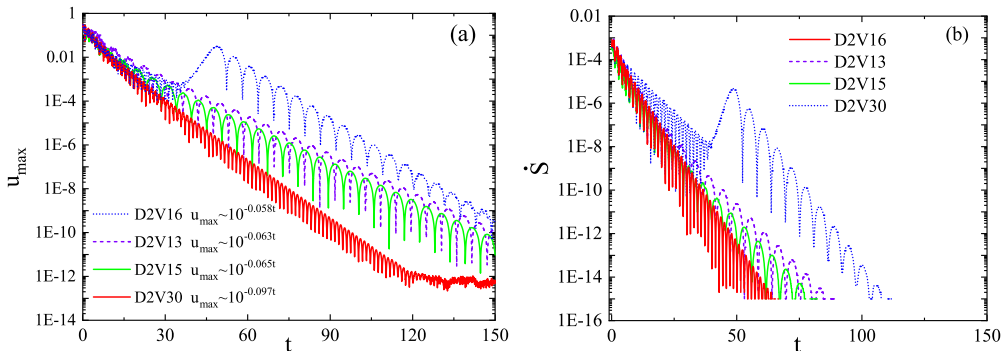


FIGURE 4. (a) Time evolutions of the maximum velocity  $u_{\max}$  calculated from various DBMs. (b) Time evolutions of entropy increase rate.

Specifically, for the D2V30 model, spurious velocity refers to the remaining current when  $t > 120$  in figure 4. The decay before  $t < 120$  is a physical process decided by the initial condition.

Discarding the early time transient regime and the very late time regime, where  $u_{\max}$  stays almost unchanged, we find,  $u_{\max}$  decreases with time  $t$  approximately in the following way:  $u_{\max} \sim 10^{-\gamma t}$ . But the exponent of the D2V30 model ( $\gamma \approx 0.1$ ) is considerably larger than that of other models ( $\gamma \sim 0.061 \pm 0.003$ ). When  $t > 120.0$ ,  $u_{\max}$  decays to a negligible value  $10^{-12}$  in D2V30 simulation under the combined effects of NOMF and NOEF. Figure 4(b) shows time evolutions of entropy increase rate for the decaying process. When the system temperature is fixed, entropy increase rate reduces to  $\frac{dS}{dt} = \int -\frac{1}{T} \Delta_2^* : \nabla \mathbf{u} d\mathbf{r}$ . The entropy increase rate reflects the speed at which the system towards equilibrium, which is qualitatively consistent with figure 4(a). The larger the entropy increase rate, the faster the decay in  $u_{\max}$ . Compared with lower-order models, a faster decay in  $u_{\max}$  obtained from the D2V30 model is due to a more accurate viscous stress the model recovers. These findings suggest that the retrieval of higher-order kinetic moments in physical modeling makes the DBM more powerful in refraining spurious currents.

### 3.1.3. Conservativeness of the new model

To examine the conservativeness of the new model, we monitor variations in  $\rho$ ,  $\rho \mathbf{u}$  and  $e_T$  in a thermal phase transition process in figure 5. The initial conditions are  $(\rho, T, u_x, u_y) = (1.5 + \Delta, 1.0, 0.0, 0.0)$ , where  $\Delta$  is a random noise of the amplitude 0.001 acting as heterogeneous nuclei and accelerating the kinetic process. The remaining parameters are  $N_x = N_y = 128$ ,  $\tau = 10^{-3}$ ,  $K = 5 \times 10^{-5}$ , and  $\text{Pr} = 0.1$ . Even when the system is instantaneously quenched to a completely unstable state, the two models maintain  $\Delta\rho$  and  $\Delta(\rho \mathbf{u})$  to machine accuracy. Meanwhile, it is found that  $\delta(\rho \mathbf{u})$  is two orders of magnitude lower than  $\delta(\rho)$ . This is because: (a)  $\delta(\rho \mathbf{u}) = u\delta\rho + \rho\delta u$ ; (b) different from the isothermal phase separation process, the release of latent heat

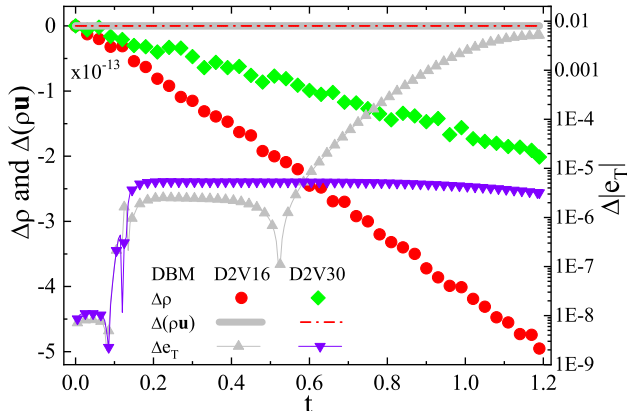


FIGURE 5. Variations in  $\rho$ ,  $\rho u$  and  $e_T$  in a thermal phase separation process obtained from D2V16 and D2V30 DBMs.

causes the changing of local temperature. The freedom in temperature results in a more detailed and stricter local mechanical and thermodynamic equilibrium, consequently hampers the full development of velocity, especially for the case with large viscosity. The mean velocity  $u_{\text{mean}}$  is approximately on the order of  $10^{-2}$  throughout the simulations we considered. So  $u\delta\rho \sim 10^{-15}$ ; (c) furthermore, it is reasonable that variations in  $\rho(t)$  and  $\rho u(t)$  are proportional to their fluctuations,  $\delta\rho \propto (\rho_{\text{max}} - \rho_{\text{min}}) \sim o(1)$  and  $\delta u \propto (u_{\text{max}} - u_{\text{min}}) \sim o(10^{-2})$ , so  $\delta u$  is two orders of magnitude lower than  $\delta\rho$ . Then  $\rho\delta u \sim 10^{-15}$ .

In our simulations, the average energy density  $e_T = \rho T - a\rho^2 + K|\nabla\rho|^2/2 + \rho u^2/2 = -3.000015$ . Different from  $\Delta\rho$  and  $\Delta(\rho u)$ ,  $\Delta e_T(t)$  oscillates and persistently grows during the whole procedure mimicked by the D2V16 model. Two reasons account for the oscillation and growth in  $\Delta e_T(t)$ . First, the appearance of numerous liquid-vapor interfaces in the spinodal decomposition stage induces macroscopic quantity gradients and accumulated spatial discretization errors. Second, the resulting macroscopic quantity gradients serve as sources of HNE and TNE which may threaten the validity of the lower-order DBM. The maximum deviation of  $e_T(t)$  is 0.01 for the D2V16 model, while  $O(10^{-6})$  for the D2V30 model, demonstrating that the D2V30 model is more effective in maintaining energy conservation and more capable of handling typical non-equilibrium processes. These variations are indicators of model accuracy, which significantly affect the phase morphology, flow field distribution, and stability of simulation.

The results for two-dimensional lattices with 13, 15, 16, and 30 velocities indicate that increasing the order of approximation of the lattice Boltzmann equation enhances performance in maintaining thermodynamic consistency, energy conservation, and refraining spurious currents.

### 3.2. Multi-scale model and trans-scale ability

In the DBM modeling, there exist two sets of macroscopic variables, the conservative set  $(\rho, \rho \mathbf{u}, e_T)$  and the non-conservative counterpart  $(\Delta_{m,n}$  and  $\Delta_{m,n}^*$ ,  $m-n \geq 2$ ), which vary in diverse time and length scales. Compared with the slowly varying conservative variables, the THNE quantities are quickly varying non-conservative ones, with extremely short relaxation times on the order of  $10^{-10}$  second (Myong 1999). In this subsection, we evaluate carefully the multi-scale predictive capability of the DBMs for describing THNE features. Specifically, we determine whether or not the DBM can correctly capture the fast-changing THNE characteristics around an evolving liquid-vapor interface. Indeed, understanding precisely the fine structure and the specific status of non-equilibrium state between two phases at coexistence is of central importance in a variety of fields, because these non-equilibrium characteristics determine the transport efficiency of mass and energy across an interface, as well as the growth dynamics and morphological behaviors.

To date, significant progresses have been made by pioneers in the non-equilibrium effects of multiphase flows. Frezzotti *et al.* comprehensively studied the rich array of non-equilibrium effects of multiphase flows through numerically solving the Enskog-Vlasov equation by DSMC (Enskog-Vlasov DSMC) and through the MD method (Frezzotti *et al.* 2005; Frezzotti 2011; Frezzotti & Rossi 2012; Frezzotti *et al.* 2018, 2019), including the non-equilibrium structure of the vapor-liquid interface, velocity slip at the liquid-vapor boundary, non-equilibrium evaporation, and non-equilibrium stress, etc. In addition to microscopic MD and mesoscopic DSMC, recently, the extended macroscopic moment method, in particular, the regularized moment method (Struchtrup & Torrilhon 2003; Struchtrup 2005; Torrilhon 2016) derived as approximations of the Boltzmann equation by means of the order-of-magnitude method has been rapidly developed and extended to the field of multiphase flows (Struchtrup *et al.* 2017; Struchtrup & Frezzotti 2022) by Struchtrup *et al.* In Struchtrup *et al.* (2017), the macroscopic evaporation boundary conditions for regularized 13 (R13) moment equations have been derived from microscopic interface conditions of the Boltzmann equation, which extends the application range of the R13 equation to multiphase flows in the transition regime. More recently, in Struchtrup & Frezzotti (2022), a set of 26 moment equations for the Enskog-Vlasov equation has been derived by using the Grad moment method, which provides a computationally efficient and functionally unified approach for ideal and non-ideal fluid flows far from equilibrium. Besides, the coupled constitutive relations theory was developed to capture the remarkable rarefaction effects at small scales in the liquid-vapor phase transition processes (Rana *et al.* 2021). Meanwhile, the rarefaction effects in a head-on collision of two identical droplets are investigated via various lattice Boltzmann models with different degrees of precision (Chen *et al.* 2022b). It is found that the rarefaction effects enhance the conversion from free energy to kinetic energy and accelerate droplet coalescence. Present *et al.* presented an original and fundamental molecular dynamics lattice gas (MDLG) approach connecting lattice Boltzmann methods

to physical reality (Parsa & Wagner 2017, 2020; Czelusniak *et al.* 2020; Parsa *et al.* 2021; Pachalieva & Wagner 2021). The key implementation of MDLG is an embedded coarse-graining procedure, i.e., mapping an MD simulation onto an LB framework. It permits to study of any system that can be simulated with MD, including the nonideal system with significant non-equilibrium fluctuations (Parsa & Wagner 2020), since the collision operator is informed by an underlying MD simulation. This approach can be considered as an optimal LBM or a more realistic coarse-grained fluctuating method. We stress that these microscopic (MD), mesoscopic (DSMC, LBM and DBM proposed here), and macroscopic (high-order moment method, extended hydrodynamics or generalized hydrodynamics models) models/methods, with different starting points and different emphases, have their own strengths and insights, complement each other, can not replace each other. In addition, the developments of these methods have stages.

Although extensive experimental and theoretical studies have been designed and developed in the past decades to address this issue (Evans 1979; Weeks 1977; Bedeaux 1986; Onuki 2002; Aarts *et al.* 2004; Lang & Leiderer 2006; Bu *et al.* 2014; Jaensson & Vermant 2018), the early stage of the liquid-vapor transition, i.e., the spinodal decomposition stage, where non-equilibrium effects are much more pronounced than the latter domain growth stage, still needs further investigations from the viewpoint of non-equilibrium thermodynamics. Early studies tend to focus on conserved quantities and slow variables, because these characteristics are relatively stable and easy to grasp (Succi 2001; Osborn *et al.* 1995; Gonnella *et al.* 1997; Xu *et al.* 2003; Gonnella *et al.* 2007; Gan *et al.* 2011, 2012b; Sofonea *et al.* 2004; Gonnella *et al.* 2010; Coclite *et al.* 2014; Onuki 2007, 2002). The study of these conserved quantities and slow variables provides a basis for the study of fast-changing behavior which is particularly relevant to the early stage of spinodal decomposition, a process still far from being completely understood.

The reason is that these fast varying and complex THNE quantities springing up in the spinodal decomposition stage are difficult to measure and analyze. Moreover, related experiments are costly and time-consuming. Theoretical analysis is usually limited to cases with numerous simplifying assumptions and generalizations, such as the local equilibrium assumption, given small deviations from the equilibrium state and linear relationship between fluxes and forces. How to overcome these limitations is a core problem in physical modeling (Gurtin & Voorhees 1996; Vilar & Rubi 2001; Schweizer *et al.* 2016; Rana *et al.* 2021).

The definition of any non-equilibrium strength depends on the perspective of the study. Complex systems need to be investigated from multiple perspectives. If we look at the system from  $N$  angles, there are  $N$  kinds of non-equilibrium strengths. Therefore, if the  $N$  kinds of non-equilibrium strengths are taken as components to introduce a non-equilibrium strength vector, it should be more accurate and specific. Below we use the

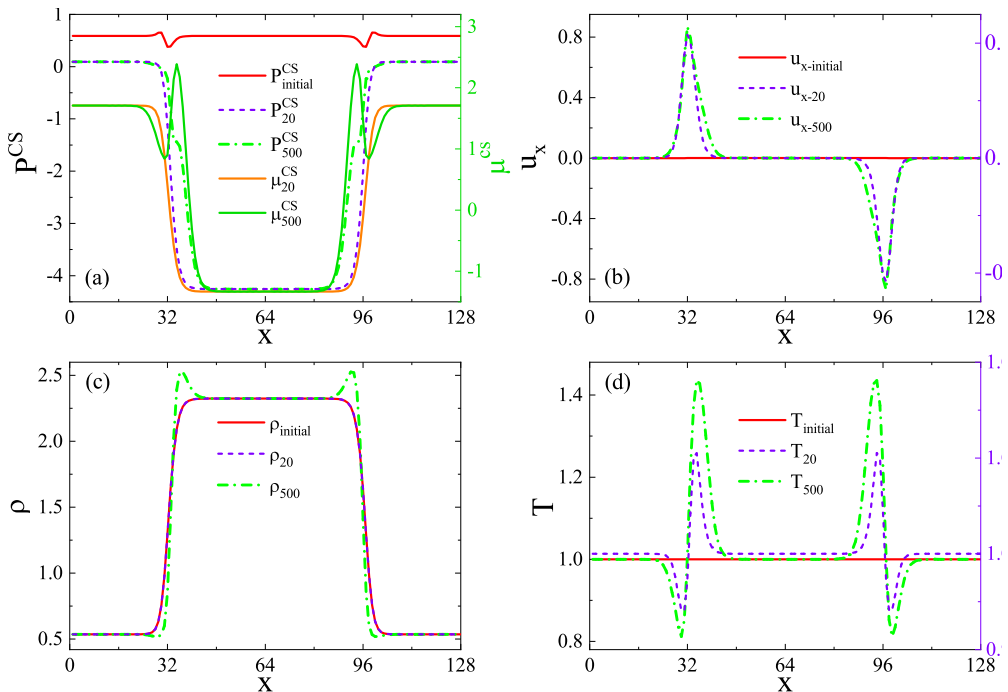


FIGURE 6. Profiles of hydrodynamic quantities calculated from the D2V30 model at three representative instants: 0, 20 and 500 iterations.

four-component vector  $\mathbf{S}_{\text{THNE}} = (\Delta_2, \Delta_{3,1}, \Delta_3, \Delta_{4,2})$ , whose analytical expressions have been derived, to roughly describe the strength of non-equilibrium.

### 3.2.1. Weak THNE case

According to the analytical formulas listed in Appendix B and Section 2.1, four explicit factors control the intensities and structures of THNE manifestations, i.e., the relaxation time  $\tau$ , the fluid velocity  $\mathbf{u}$ , the gradient force and interparticle force caused by gradients of macroscopic quantities (GMQs). GMQs are implicitly affected by the initial state and the duration of evolution, for example, the initial density distribution, the quenching temperature, the surface tension coefficient, and the Prandtl number, etc. Therefore, by adjusting these aspects, we can design scenarios with weak, moderate, and strong THNE strengths.

First, we investigate the weak THNE case. The initial state is the equilibrium density profile  $\rho_{\text{initial}}(x)$  at  $T = 1.74$ , as shown in panel (c) of figure 6. The parameters are as follows  $K = 2.7 \times 10^{-5}$ ,  $\Delta t = 2 \times 10^{-5}$ ,  $\Delta x = \Delta y = 5 \times 10^{-3}$ , others are consistent with those in figure 3. When simulation starts, the system is suddenly quenched to  $T = 1.0$ . The profiles of hydrodynamic quantities, including the chemical potential (Wagner 2006; Wen *et al.* 2017, 2020)  $\mu^{\text{CS}} = RT[\frac{3-b\rho/4}{(1-b\rho/4)^3} + \ln \rho + 1] - 2a\rho - K\nabla^2\rho$ , calculated from the D2V30 model at representative instants are shown in figure 6, where  $\phi_n$  represents the macroscopic quantity after  $n$  iterations. The following results have been obtained: (i)

the instantaneous decrease in temperature results in the emergence of steep gradients in both pressure  $P^{\text{CS}}$  and chemical potential  $\mu^{\text{CS}}$  near the liquid-vapor interfaces [see panel (a)]; (ii) the pressure and chemical potential gradients drive the vapor phase across the interface towards the liquid phase [see panels (b) and (c)], contributing to the decrease (increase) in vapor (liquid) density, and the appearance of remarkable velocity around the interface. After 20 iterations, the maximum velocity along the  $x$  direction  $u_{x\text{-max}}$  is approximately 0.04, but exceeds 0.80 after 500 iterations; (iii) with the development of phase separation, latent heat is locally released to and absorbed by the surrounding liquid and vapor phases, respectively. These processes lead to violent changes in temperature and local mechanical imbalance. The maximum temperature difference between the two phases  $\Delta T_{\text{max}}$  is negligible at the very beginning of the procedure, but reaches  $0.6T_{\text{initial}}$  at  $t = 0.01$  (500 iterations), which is the largest difference from an isothermal case at a fixed temperature.

Figure 7 portrays the specific THNE manifestations  $\Delta_{2xx}$ ,  $\Delta_{3,1x}$ ,  $\Delta_{3xxx}$ , and  $\Delta_{4,2xx}$  for figure 6 at  $t = 4 \times 10^{-4}$  (20 iterations), where the D2V13 model at the NS level (left column), the D2V15 model at the NS level (middle column), and the D2V30 model beyond the third-order super-Burnett level (right column) have been adopted. For the convenience of comparisons, analytical solutions with the first and second-order accuracies are plotted in each panel by solid lines. Figure 7 shows the general characteristics when the system deviates from thermo-hydrodynamic equilibrium: (i) THNE effects primarily concentrate in the interfacial regions, where the interparticle force and gradient force dominate, and disappear in the same manner as the GMQs vanish in the liquid and vapor bulk phases. (ii) Owing to the limited action time of the gradient force and interparticle force, THNE effects are not fully developed until this moment. (iii) The first-order THNE  $\Delta_{m,n}^{(1)} \propto \tau$ , is always larger than the second-order THNE  $\Delta_{m,n}^{(2)} \propto \tau^2$ , demonstrating that  $\Delta_{m,n}^{(1)}$  is the principal part of  $\Delta_{m,n}$  and, to some extent, the effectiveness of the lower-order coarse-grained model. (iv) It is interesting to find that  $|\Delta_{m,n}^{(1)} + \Delta_{m,n}^{(2)}|$  is not larger than  $|\Delta_{m,n}^{(1)}|$ , i.e., the second-order THNE invariably acts as negative feedback on the first-order one, and weakens the total THNE intensity.

Beyond the aforementioned commonalities, the following distinctive performances among various models should be thoroughly examined. It is clear that, even with such a feeble THNE, the simulation results of D2V13 and D2V15 models do not match well, either with the first-order or the second-order theoretical solutions. More explicitly, the two lower-order models tremendously overestimate the THNE level, especially on the vapor side and for the  $xxx$  component of  $\Delta_3$ . The discrepancies possess peak values approximately at the locations where the gradient of the most associated physical quantity reaches its local maximum (minimum).

Two key factors are responsible for the failure of the lower-order DBM in capturing THNE accurately. On the one hand, to fully describe a given non-equilibrium quantity  $\Delta_{m,n}^{(j)}$ , the number of the required kinetic moments exactly retrieved by the discrete



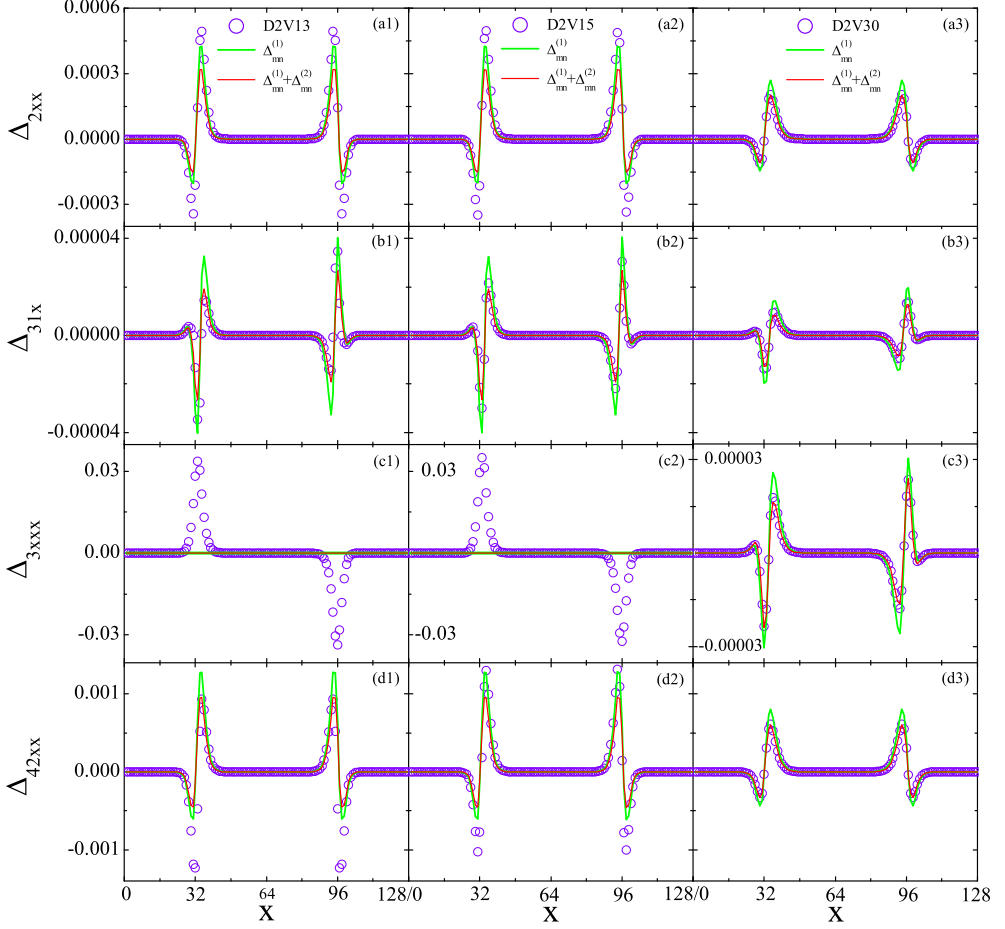


FIGURE 7. Weak case: THNE manifestations calculated from DBMs at various levels and theoretical analysis. Here  $t = 4 \times 10^{-4}$  (20 iterations) and  $\tau = 10^{-4}$ .

equilibrium distribution function  $f_i^{(0)}$  increases with increasing  $m$ , i.e., the rank of  $\Delta_{m,n}$ . As shown in Table 1, in the formulation of  $\Delta_{3,1}^{(1)}$ ,  $f_i^{(0)}$  should satisfy the moment  $\mathbf{M}_{5,1}$ ; when deriving  $\Delta_{4,2}^{(1)}$ ,  $f_i^{(0)}$  should satisfy higher-order moments  $\mathbf{M}_{5,3}$  and  $\mathbf{M}_{6,2}$ . On the other hand, additional moment constraints on  $f_i^{(0)}$  need to be selected and guaranteed with increasing  $j$ , i.e., the order of accuracy of  $\Delta_{m,n}$ . Concretely, a first-order accuracy in the description of  $\Delta_3$  can be achieved by maintaining  $\mathbf{M}_4$  and  $\mathbf{M}_5$ ; while realizing a second-order accuracy in the description of  $\Delta_3$ ,  $f_i^{(0)}$  should further retain the additional thermodynamic one  $\mathbf{M}_{6,4}$  ( $\mathbf{M}_{5,3}$ , in the 6th line of Table 1, is not independent of  $\mathbf{M}_5$ ). Table 2 manifests that both the D2V13 and D2V15 models cannot hold these necessary constraint relationships, even just for the first-order accurate descriptions of  $\Delta_{3,1}^{(1)}$  and  $\Delta_{4,2}^{(1)}$ . Among these THNE quantities, the correct description of  $\Delta_3$  and  $\Delta_{4,2}$  requires the retrieval of the highest order moment relations. Thus, as expected, the worst simulation results appear in panels (c1), c(2), d(1), and d(2), provided by the two lower-order models.

Compared with the D2V13 model, the supplemental moment  $\mathbf{M}_{5,1}$  which is necessary for the formulation of  $\Delta_{3,1}^{(1)}$  and maintained by the D2V15 model, plays a fairly negligible role in improving the numerical precision of  $\Delta_{3,1x}$ , because the second-order non-equilibrium effects  $\Delta_{m,n}^{(2)}$  cannot be neglected in contrast to the first-order  $\Delta_{m,n}^{(1)}$  during the early stage of spinodal decomposition. Under this condition, considering the first-order THNE effects only is not recommended. Indeed, at the beginning of the phase separation, the gradients of temperature and velocity approximately equal to zero. As a result,  $\Delta_{2xx}^{(1)} \simeq 0$ , and  $\Delta_{2xx}^{(2)}$  can be simplified to  $\frac{T^2}{\rho}(\partial_x \rho)^2 - T^2(\frac{\partial^2 \rho}{\partial^2 x}) - \rho T^2 \partial_x B_x$ . These higher-order terms in  $\Delta_{2xx}^{(2)}$  do not appear in classical hydrodynamics, but is essential for modeling system far-from-equilibrium (Struchtrup 2005; Struchtrup & Frezzotti 2022). Other non-equilibrium measures can be analyzed similarly. That is, interparticle force and density gradient force first trigger the second-order THNE, and afterward, stimulate the first-order THNE through enlarging velocity and temperature gradients. To evaluate under which circumstances the higher-order THNE should be taken into account, a characteristic dimensionless parameter, called the relative THNE strength  $R_{\text{THNE}} = |\Delta_{m,n}^{(j+1)} / \Delta_{m,n}^{(j)}|$ , may be introduced for the estimation of the relative importance of the  $(j+1)$ -th order THNE effects to the  $j$ -th order one. The  $R_{\text{THNE}}$  for  $\Delta_{2xx}$ ,  $\Delta_{3,1x}$ ,  $\Delta_{3xxx}$ , and  $\Delta_{4,2xx}$  at the positions where these non-equilibrium measures own extreme values, are 0.250, 0.349, 0.212, and 0.252, respectively. At earlier times, such as after 15 iterations,  $R_{\text{THNE}}$  is as high as 0.50. Therefore, higher-order DBMs with at least second-order accuracy for  $\Delta_{m,n}$ , are undoubtedly needed, even for cases with faint non-equilibrium effects. Tables 1 and 2 indicate that the D2V30 model satisfies all the needed kinetic moment relations. Consequently, the D2V30 results are consistent with the theoretical analysis at the second-order of accuracy. Particularly, the remarkable deviations in panels (c1) and (c2) disappear in panel (c3).

### 3.2.2. Moderate THNE case

As time evolves, the degree of phase separation becomes pronounced, with extended phase-separating regions and prominent gradients of macroscopic quantities (see dash-dot lines in figure 6). The non-equilibrium manifestations at the same instant, exhibited in figure 8, indicate that the system enters into the moderate THNE stage. Compared with figure 7, the most distinctive difference in figure 8 is the enormous growth in  $\Delta_{m,n}$ , approximately  $10 \sim 1000$  times larger than those in the weak case. For each kind of THNE quantity, the first-order analytical solution (denoted by big green dots) overlaps with the second-order one (denoted by red solid lines), illustrating that  $\Delta_{m,n}^{(2)}$  is negligible compared with  $\Delta_{m,n}^{(1)}$ . Correspondingly, the relative THNE strength  $R_{\text{THNE}}$  for  $\Delta_{2xx}$ ,  $\Delta_{3,1x}$ ,  $\Delta_{3xxx}$ , and  $\Delta_{4,2xx}$  are as small as 0.006, 0.002, 0.018, and 0.016, respectively. For  $\Delta_{2xx}$ , good agreements between simulations and theoretical solutions are depicted in panels (a1) and (a2). This is understandable because either the D2V13 or D2V15 model is a sufficient description of  $\Delta_{2xx}^{(1)}$ . Nevertheless, for  $\Delta_{3,1x}$ , owing to the lack of

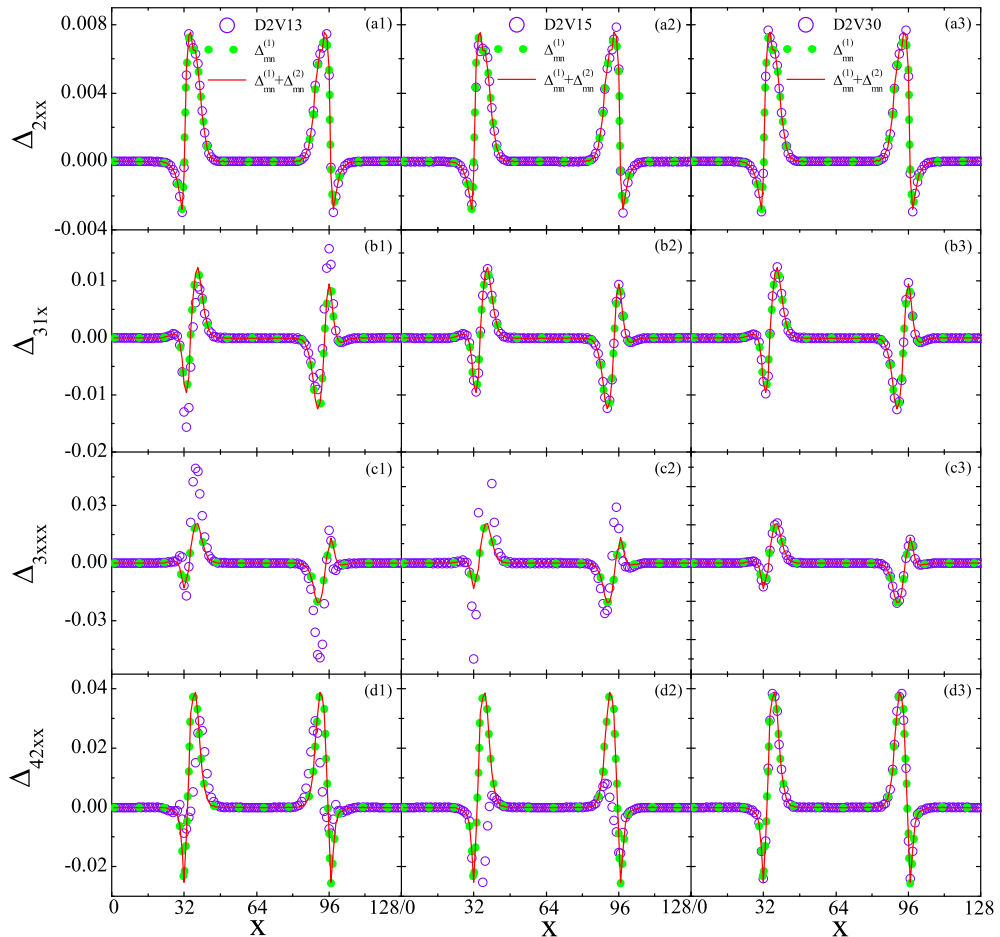


FIGURE 8. Moderate case: non-equilibrium manifestations calculated from DBMs at various levels and theoretical analysis. Here  $t = 0.01$  (500 iterations) and  $\tau = 10^{-4}$ .

indispensable kinetic moment  $\mathbf{M}_{5,1}$  in the D2V13 model, distinct discrepancies are found in panel (b1); but are absent in panel (b2), obtained from the D2V15 model that meets the constraint of  $\mathbf{M}_{5,1}$ . Similarly, for  $\Delta_{3xxx}$  and  $\Delta_{4,2xx}$ , the D2V13 and D2V15 results mismatch the theoretical profiles, because of the deficiencies in the necessary high order moments  $\mathbf{M}_4$ ,  $\mathbf{M}_5$ , and  $\mathbf{M}_{6,2}$ . By contrast, as shown in the third column of figure 8, the D2V30 results excellently coincide with the theoretical results, regardless of the relative non-equilibrium intensity. We also stress that, if we focus only on the hydrodynamic quantities and constitutive relations (related to  $\Delta_2$  and  $\Delta_{3,1}$ ), but not the evolution of the constitutive relations (related to  $\Delta_3$  and  $\Delta_{4,2}$ ), the D2V15 model is reliable and acceptable when  $R_{\text{THNE}}$  is small enough.

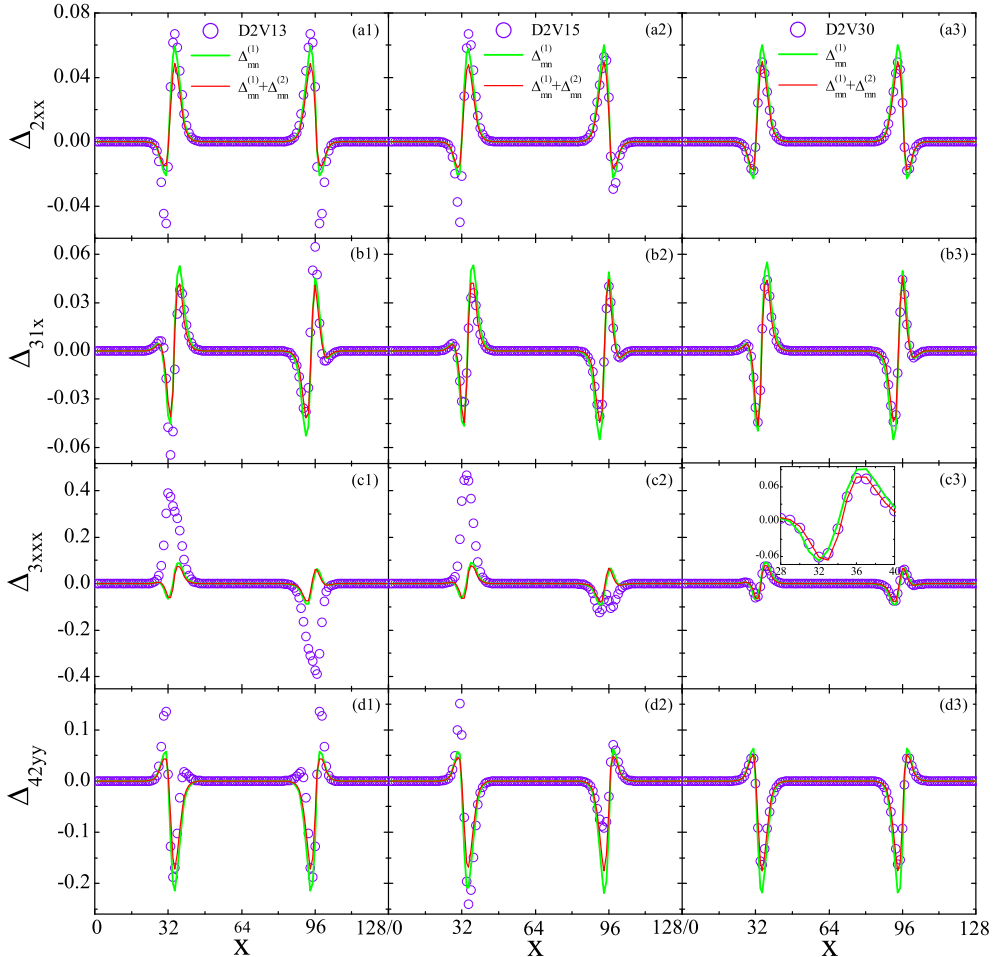


FIGURE 9. Strong case: non-equilibrium manifestations calculated from DBMs at various levels and theoretical analysis. Here  $t = 0.006$  (300 iterations) and  $\tau = 10^{-3}$ .

### 3.2.3. Strong THNE case

To further examine the multi-scale ability of the models, we increase the strength of THNE measures by straightforwardly increasing the relaxation time  $\tau$  in figure 9. In addition, another way to control the THNE strength is by adjusting the quenching depth  $T/T_C$ , which indirectly affects the non-equilibrium intensity by changing the gradients of hydrodynamic quantities. With the increasing of THNE intensity, deviations between lower-order DBM simulations and theoretical solutions become extraordinarily conspicuous (see the first and second columns of figure 9). The relative THNE strength  $R_{\text{THNE}}$  for  $\Delta_{2xx}$ ,  $\Delta_{3,1x}$ ,  $\Delta_{3xxx}$ , and  $\Delta_{4,2yy}$  rapidly reach up to 0.213, 0.248, 0.169, and 0.239, respectively, manifesting the importance of the second-order THNE and the urgent need for a higher-order DBM. The D2V30 model meets the minimum physical requirements in accurately describing the concerned THNE quantities. Therefore, the reasonable

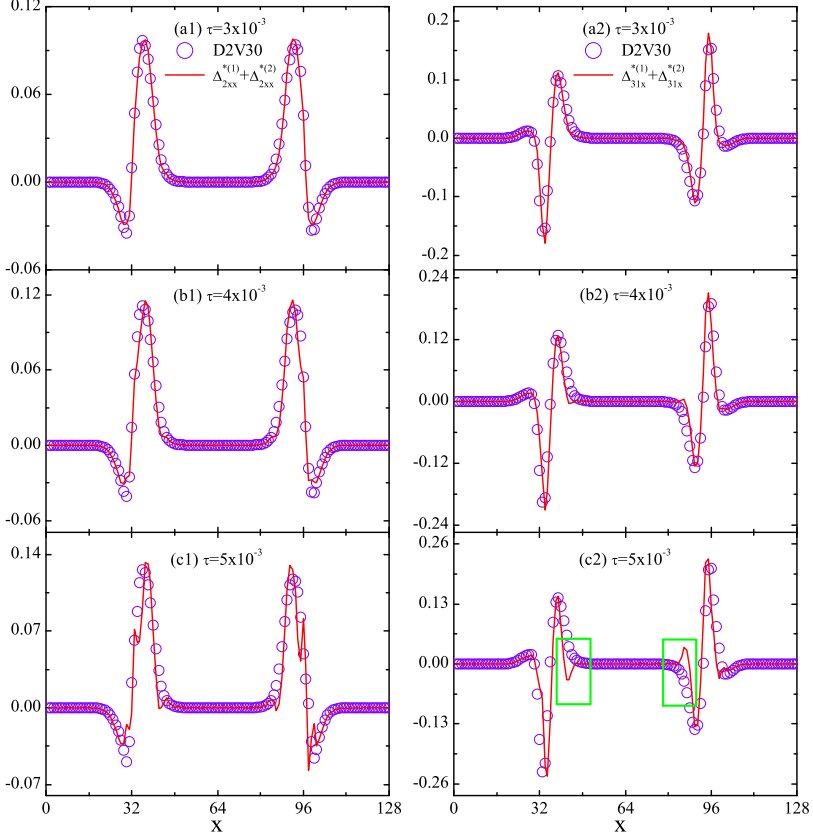


FIGURE 10. Effects of relaxation time on typical TNE manifestations: Viscous stress (left column) and heat flux (right column).

agreements between D2V30 simulations and corresponding theoretical solutions in the weak, moderate and strong THNE cases comprehensively demonstrate that the D2V30 DBM is indeed a multi-scale model and possesses better trans-scale ability than the D2V13 and D2V15 models.

To assess the application range of the DBM more completely, we resort to the Knudsen number, a dimensionless parameter generally used to characterize non-equilibrium or rarefaction degree of flows, and classify various flow regimes. The Knudsen number  $Kn = \lambda/L$ , defined as the ratio of the mean free path  $\lambda = c_s \tau$  to a characteristic length we focus on  $L = \theta/|\nabla\theta|$ , where  $c_s$  is the local speed of sound,  $\theta$  a physical quantity. The maximum  $Kn_{\max}$  calculated by density for cases with weak, moderate, and strong THNE effects are 0.008, 0.015, and 0.141, respectively, all beyond the application scope of NS equations. Evidently, the applicable range of the D2V30 model has been extended into the early transition regime.

### 3.3. Effects of relaxation time on TNE

In this subsection, we investigate the multi-scale limit of the D2V30 model through exploring whether the model can correctly reproduce higher-order constitutive relations for multiphase flows over a wide range of relaxation times and Knudsen numbers. Essentially, the accurate description of constitutive relations is of fundamental importance to the simulation of highly non-equilibrium multiphase flows (Struchtrup 2005). It is the constitutive relations that directly determine the multi-scale ability and accuracy of a model. For this purpose, in figure 10, we exhibit the effects of relaxation time  $\tau$  on the two typical TNE manifestations: viscous stress (left column) and heat flux (right column) at  $t = 0.01$ , where the initial conditions and parameters in figure 7 are used, except for  $K = 5 \times 10^{-5}$ . To be seen is that, the magnitudes of  $\Delta_{2xx}^*$ ,  $\Delta_{3,1x}^*$ , and the discrepancies between DBM simulations and the second-order theoretical solutions, increase as  $\tau$  increases. Specifically, for the case with  $\tau = 3 \times 10^{-3}$ , excellent coincidences can be observed between the two counterparts; when  $\tau$  increases to  $4 \times 10^{-3}$ , good agreements can be found; whereas when  $\tau$  further increases to  $5 \times 10^{-3}$ , noticeable oscillations and distinctions, labeled by green rectangles, emerge around the interfaces in panels (c1) and (c2), respectively.

Apart from the relative TNE intensity  $R_{\text{TNE}} = |\Delta_{m,n}^{*(j+1)} / \Delta_{m,n}^{*(j)}|$ , the aforementioned TNE discrepancy between DBM simulation and theoretical solution,  $\varkappa_{\text{Dis}} = \Delta_{\text{DBM}}^* - \Delta_{\text{Exact}}^*$ , or the relative TNE discrepancy  $R_{\text{Dis}} = |(\Delta_{\text{DBM}}^* - \Delta_{\text{Exact}}^*) / \Delta_{\text{Exact}}^*|$  can be regarded as a non-equilibrium criterion for assessing the effectiveness of a coarse-grained model and appropriateness of the coarse-graining process, as shown in Section 2. In real simulations, only when  $R_{\text{TNE}}$  or  $R_{\text{Dis}}$  is negligibly small, the proposed DBM is physically sufficient and appropriate. Otherwise, higher-order DBM that considers higher-order TNE effects should be adopted. Thus, from this point of view, the critical relaxation time for D2V30 model is  $\tau_C = 4 \times 10^{-3}$  with respect to this standard test. When  $\tau > \tau_C$ , the present model is ineffective and unacceptable, contributions of high order departures from equilibrium distribution function  $f^{(j)}$  ( $j > 2$ ) should be considered in physical modeling.

Figure 11 further demonstrates that higher-order constitutive relations are necessary for obtaining accurate hydrodynamic quantities and fine structures of material and mechanical interfaces as the degree of non-equilibrium deepens ( $\tau = 4 \times 10^{-3}$ ), where  $\varphi_M - \varphi_N$  represents hydrodynamic quantity difference calculated from models with  $M$  and  $N$  discrete velocities. The maximum relative error in the velocity profile is 28.4% at this moment, typically located at the highly non-equilibrium regime, but quickly reaches up to 70.0% after 200 iterations with the accumulation of errors. This kind of error, belonging to the physical modeling aspect, cannot be reduced or eliminated by improving the accuracy of the algorithm. The inaccuracy of D2V13 and D2V15 models is due to the crucial missing of some necessary higher-order moments required for recovering  $f^{(j)}$  ( $j \geq 2$ ).

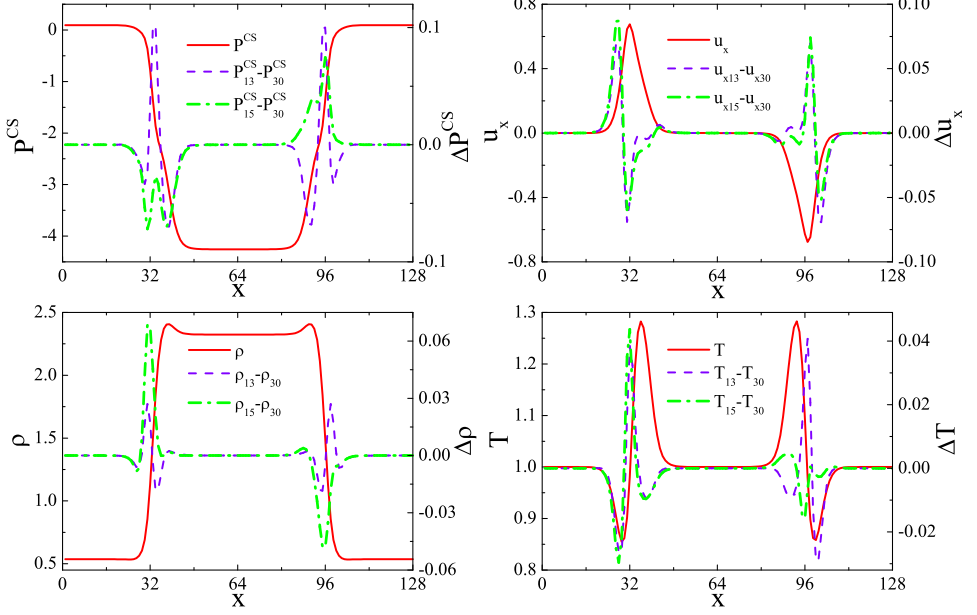


FIGURE 11. Hydrodynamic quantities calculated from the D2V30 model, and the corresponding differences among D2V30, D2V15 and D2V13 models at  $t = 0.01$  when  $\tau = 4 \times 10^{-3}$ .

Subsequently, we illustrate the effects of relaxation time on the slowly and quickly varying variables in figure 12. The first two panels in figure 12 demonstrates how relaxation time  $\tau$  affects the maximum viscous stress  $\Delta_{2xx-\max}^*$  and the maximum heat flux  $\Delta_{3,1x-\max}^*$ . Clearly,  $\tau$  strengthens the intensities of  $\Delta_{2xx-\max}^*$  and  $\Delta_{3,1x-\max}^*$  in the same manner. The relationship between  $\Delta_{2xx-\max}^*$  ( $\Delta_{3,1x-\max}^*$ ) and  $\tau$  can be divided into two stages: linear and nonlinear. When  $\tau \leq \tau_0$ ,  $\Delta_{2xx-\max}^*$  ( $\Delta_{3,1x-\max}^*$ ) increases linearly with  $\tau$ ,  $\Delta_{2xx-\max}^* = B_2\tau$  ( $\Delta_{3,1x-\max}^* = B_4\tau$ ); when  $\tau > \tau_0$ , the linearization is no longer valid, the dependence of  $\Delta_{2xx-\max}^*$  ( $\Delta_{3,1x-\max}^*$ ) on  $\tau$  can be fitted by  $\Delta_{2xx-\max}^* = A_1 + B_1\tau^{2/3}$  ( $\Delta_{3,1x-\max}^* = A_3 + B_3\tau^{2/3}$ ), manifesting the necessity of higher-order constitutive relations for a system far-away-from equilibrium. The fitting parameters are  $A_1 = -0.006$ ,  $B_1 = 4.889$ ,  $B_2 = 45.000$ ,  $A_3 = -0.014$ ,  $B_3 = 8.231$ ,  $B_4 = 69.291$ . Of course, the ending point of the linear constitutive relations provides a distinct criterion to identify whether the system is near or far from equilibrium. Panel (c) shows distributions of the local Knudsen number  $Kn(x)$  with various  $\tau$ . Similar to the behaviors of THNE,  $Kn(x)$  becomes more pronounced in the interfacial region and reach its maximum at the point at which the gradient of quantity attains its peak value; and vanishes exponentially in the bulk of the liquid and vapor regions. The maximum interface Knudsen number  $Kn_{\max}$  calculated from density exceeds  $1/3$ , indicating that the D2V30 model is valid in the transition flow regime. Different from the ideal gas system and the effects of surface tension, the relaxation time  $\tau$  only enlarges the amplitude of  $Kn$ , but does not extend the non-equilibrium region, or broaden the characteristic length scale

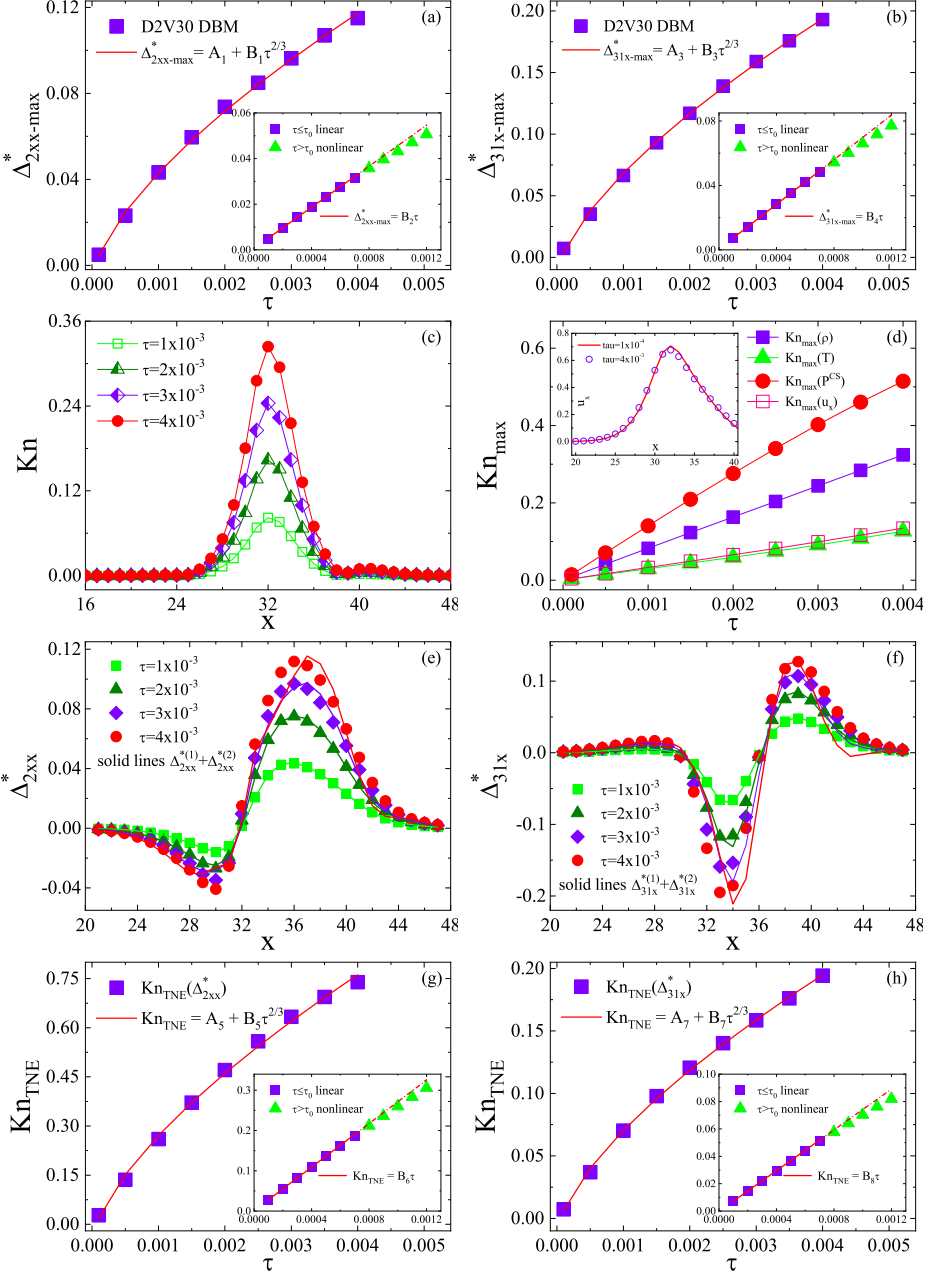


FIGURE 12. Effects of relaxation time on the maximum viscous stress (a), the maximum heat flux (b), distributions of the local Knudsen number (c), the maximum Knudsen number (d), distributions of viscous stress (e), distributions of heat flux (f), the Knudsen number calculated from viscous stress (g), and the Knudsen number calculated from heat flux (h).

of a system, resulting in the approximately linear dependence of  $Kn_{max}(\rho, T, P^{cs}, u_x)$  on  $\tau$ , as shown in panel (d). This is because the slowly varying variables appear to be slightly affected [for  $u_x(x)$ , see the legend of figure 12(d)], or basically unaffected [for  $\rho(x)$ ,



$T(x)$ ,  $P^{CS}(x)$ , not shown here] by relaxation time until this moment, but noteworthy smoothed by the surface tension coefficient [see figures 13(c)-(d)]. From this perspective, the interface Knudsen number calculated from the slowly varying quantity cannot be viewed as a qualified parameter to characterize the non-equilibrium behaviors at the early stage of phase separation.

To solve this issue, we therefore resort to the quickly varying quantities, i.e., the TNE measures, and Knudsen numbers calculated from them. Figures 12(e)-(f) show effects of the relaxation time on viscous stresses and heat fluxes, where scatter symbols represent DBM simulation results, solid lines indicate the corresponding theoretical estimates. As shown in panels (e) and (f), the relaxation time substantially improves the magnitudes of TNE measures and changes their structures. The characteristic length scales are extraordinarily sensitive to relaxation time, position and time. The last two panels suggest that the relaxation time significantly enhances the maximum Knudsen numbers calculated from viscous stress  $Kn_{\max}(\Delta_{2xx}^*)$  (g) and heat flux  $Kn_{\max}(\Delta_{3,1x}^*)$  (h). The  $Kn_{\text{TNE}} \sim \tau$  relation behaves qualitatively similar to the one between  $\Delta_{2xx-\max}^*$  ( $\Delta_{3,1x-\max}^*$ ) and  $\tau$ . The moderate growth in  $Kn_{\text{TNE}}$  when  $\tau > \tau_0$  results from the second-order TNE effect that refrains the total TNE intensity.

### 3.4. Effects of surface tension on TNE

Here, the focus is on how and to what extent surface tension affects the dynamic patterns and TNE features. Figures 13(a)-(b) show the viscous stresses and heat fluxes at  $t = 0.01$  for cases with various surface tension coefficients  $K$ , where symbols stand for simulation results, and solid lines in panels (a)-(b) and their legends represent the corresponding second-order analytical solutions. The initial conditions and other parameters are the same as those in figure 9. As shown, the surface tension effects are threefold, refraining the local TNE intensity near the interface, but expanding the TNE range and strengthening the TNE intensity away from the interface (see the solid lines and the red arrows in legends for details), through interface smoothing and extending. This result can also be verified by figures 13(c)-(d), where the maximum of  $Kn$  decreases but the region with non-zero  $Kn$  increases with  $K$ , as a result of the capillary wave broadening. When  $K$  varies in the interval  $[3 \times 10^{-5}, 18 \times 10^{-5}]$ , the dependence of  $Kn_{\max}(\rho)$  and  $Kn_{\max}(T)$  on  $K$  can be fitted by  $Kn_{\max}(\rho) = A_9 + B_9/K$  and  $Kn_{\max}(T) = A_{10} + B_{10}/K$ , respectively, with  $A_9 = 0.013$ ,  $B_9 = 3.422 \times 10^{-6}$ ,  $A_{10} = -0.003$ , and  $B_{10} = 1.588 \times 10^{-6}$ . The high sensitivity of density profile to surface tension coefficient [see the legend of figure 13(d)] is mainly due to the  $\Lambda$  term in (2.2) which is linearly proportional to  $K$ .

Accordingly, as plotted in figures 13(e)-(f), the maxima of  $\Delta_{2xx}^*$  and  $\Delta_{3,1x}^*$  decrease synchronously with  $K$  approximately in the following way,  $\Delta_{2xx-\max}^* = A_{11} + B_{11}/K^{1/2}$  and  $\Delta_{3,1-\max}^* = A_{12} + B_{12}/K$ , with  $A_{11} = -0.023$ ,  $B_{11} = 4.667 \times 10^{-4}$ ,  $A_{12} = 0.008$ , and  $B_{12} = 3.711 \times 10^{-6}$ . In other words, large resistances to mass and heat transfers appear

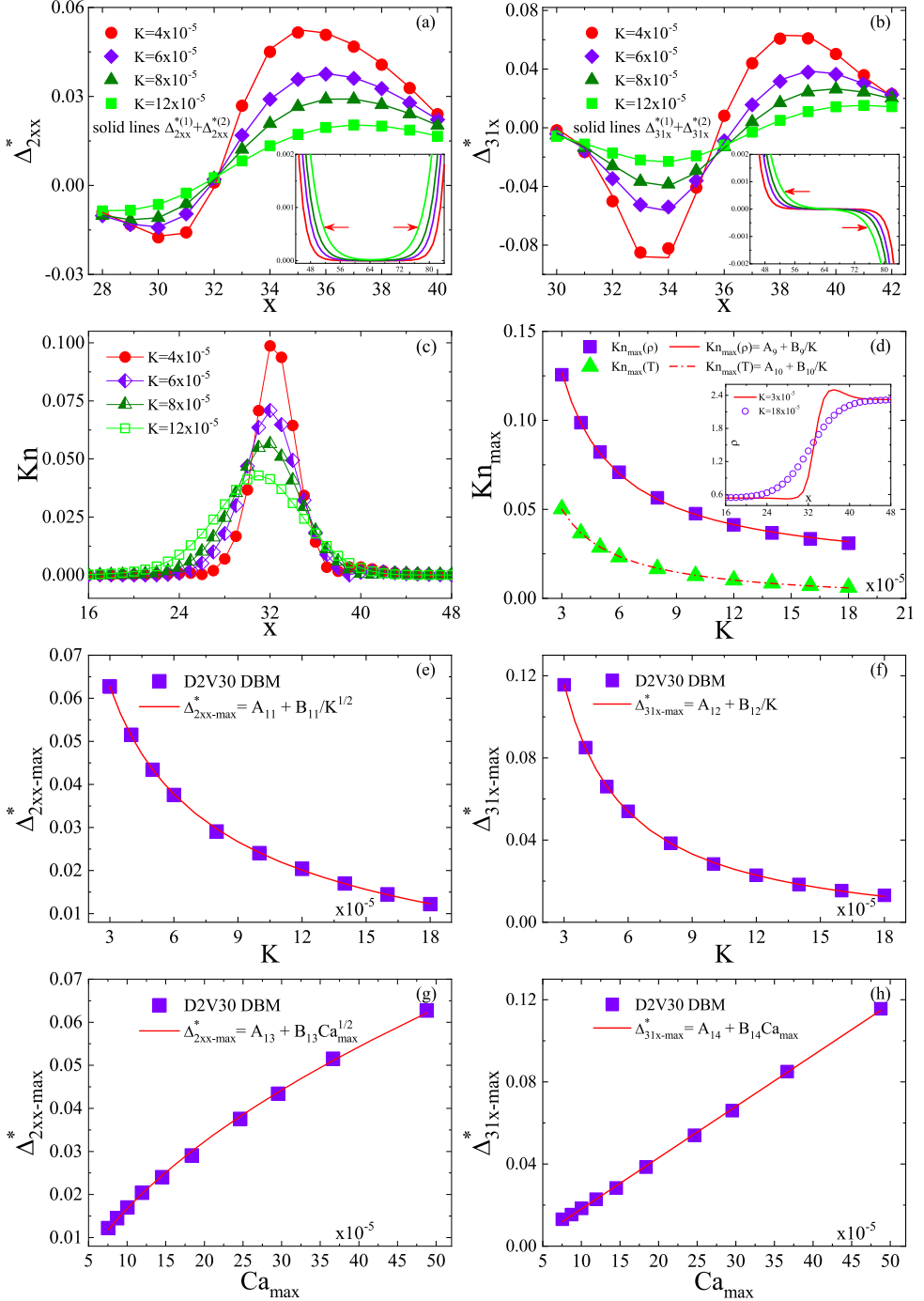


FIGURE 13. Effects of surface tension coefficient on the distributions of viscous stress (a), heat flux (b), and the local Knudsen number (c), the maximum of Knudsen numbers calculated from density and temperature (d), the maximum viscous stress (e) and the maximum heat flux (f). Relation between the maximum viscous stress and the maximum Capillary number (g), the relation between the maximum DBM heat flux and the maximum Capillary number (h).

at the interface, and increase with the surface tension coefficient. The suppressive effect of surface tension on heat flux is much stronger than that on viscous stress at a small Prandtl number. We further examine the effects of surface tension on TNE in terms of the Capillary number  $Ca$ , which denotes the ratio between viscous force and interfacial tension,  $Ca = \mu u_C / \sigma$ , with  $u_C$  the characteristic velocity and  $\sigma$  the interfacial tension between liquid and vapor phases. For a planar interface,  $\sigma$  can be specifically computed as  $\sigma = K \int_{-\infty}^{\infty} (\frac{\partial \rho}{\partial z})^2 dz$ . Figures 13(g) and (h) show relations among TNE measures and the maximum Capillary number  $Ca_{\max}$ . Clearly,  $\Delta_{2xx-\max}^*$  and  $\Delta_{3,1x-\max}^*$  increase with increasing  $Ca_{\max}$ . The two relations can be fitted by  $\Delta_{2xx-\max}^* = A_{13} + B_{13} Ca_{\max}^{1/2}$  and  $\Delta_{3,1-\max}^* = A_{14} + B_{14} Ca_{\max}$ , with fitting parameters  $A_{13} = -0.021$ ,  $B_{13} = 3.761$ ,  $A_{14} = -0.007$ , and  $B_{14} = 249.513$ . The diametrically opposite trends in panels (e) and (g) [also panels (f) and (h)] are due to the inverse relation between  $Ca_{\max}$  and  $K$ ,  $Ca_{\max} \sim K^{-1}$ .

#### 4. Conclusions and remarks

From the perspective of kinetic theory, the transport properties of a flowing system are described by the distribution function  $f$  or by the full sequence of its kinetic moments. The conservative kinetic moments of  $f$  include the density, momentum, and energy. Acquisition of these conservative kinetic moments is equivalent to knowing only the equilibrium distribution function  $f^{(0)}$ , namely perfect fluids free from dissipative effects. How and to what extent the system deviates from the thermodynamic equilibrium remains completely unknown at this stage.

To know the distribution function  $f$  is equivalent to knowing all the kinetic moments of  $f$ , which is neither possible nor necessary for the vast majority of situations. Which kinetic moments need to be known for multi-scale modeling of complex flows is the first key question that DBM endeavors to address. The second is how to detect, describe, present, and analyze THNE states. Along this line, we present a framework for constructing multi-scale discrete Boltzmann models for thermal multiphase flows ranging from continuum to transition flow regimes. The DBM is a straightforward and efficient kinetic moment-matching method, whose basic framework consists of three fundamental steps: (i) establishment of the formal links with the modified continuous Boltzmann-BGK equation, the extended hydrodynamic equations and the sought thermo-hydrodynamic non-equilibrium phenomena under consideration, (ii) formulation of the thermo-hydrodynamic non-equilibrium measures, and (iii) discretization of the particle velocity space for the construction of the discrete equilibrium distribution function. In addition, phase space manifolds spanned by the independent components of non-conservative kinetic moments of  $(f - f^{(0)})$  are introduced to describe the corresponding non-equilibrium states and effects. The concept of metric distance from the origin in such phase space is extended to intuitively describe the non-equilibrium depth. The concept of

metric distance between two points in such phase space is extended to intuitively describe the difference between two states.

In the case of the validity of Chapman-Enskog theory, step (ii) permits to select the minimum physical requirements for describing the thermo-hydrodynamic non-equilibrium quantities of interest to the desired order of accuracy, that is, it determines the fewest required kinetic moments  $\Phi_n = (\mathbf{M}_0, \mathbf{M}_1, \dots, \mathbf{M}_n)^T$  that the discrete equilibrium distribution function should retrieve during the coarse-grained physical modeling process. It also provides valuable byproducts: Higher-order constitutive relations and the most relevant higher-order thermo-hydrodynamic non-equilibrium manifestations which are expected to improve the macroscopic modeling and enhance the understanding of dynamic constitutive relations.

The set of the fewest kinetic moments offers a unique perspective to investigate the non-equilibrium behavior of the “mesoscale” or “dilemma” situations where the continuum modeling fails and the molecular dynamics method lacks sufficient power to reach up to the scales of interest. The research perspective and modeling accuracy depend on the specific elements of moment sets, and can be adjusted and improved in time. For instance, to access stronger non-equilibrium effects, one needs to include more higher-order moment relations into  $\Phi_n$ , so that the discrete Boltzmann model becomes more consistent with the continuous Boltzmann equation far from equilibrium. Importantly, the computational complexity of the DBM increases only mildly in the process, as opposed to the case of generalized hydrodynamics, such as the Burnett or the super-Burnett equations.

As model examples, two-dimensional discrete Boltzmann models with 13, 15 and 30 discrete velocities at Navier-Stokes and beyond Burnett levels have been proposed and evaluated. It is found that the incorporation of additional higher-order kinetic moments helps to enhance the liquid-vapor density ratio that the model can hold, to curb spurious currents around the interface, and to ensure better mass, momentum, and energy conservation in phase-separating systems. The multi-scale predictive capability of the discrete Boltzmann model to describe thermo-hydrodynamic non-equilibrium features increases with the number of independent kinetic moments included by the model. As fast varying variables, the thermodynamic and thermo-hydrodynamic non-equilibrium measures provide more detailed information on the non-equilibrium multiphase flow system than methods based on macroscopic conserved quantities alone, thereby shedding new light on these complex states of flowing matter far from equilibrium. Future work includes a more complete comparison among DBM results, high-order moment method (Struchtrup *et al.* 2017; Struchtrup & Frezzotti 2022) and particle-based method (Frezzotti *et al.* 2005; Frezzotti 2011; Frezzotti & Rossi 2012; Frezzotti *et al.* 2018, 2019); the incorporation of the external force in a more fundamental way, construction of appropriate kinetic boundary conditions (Frezzotti 2011; Struchtrup *et al.* 2017; Zhang *et al.* 2022b), and consideration of the case with faster phase separation, say the phase transition time scale is comparable to the molecular thermal relaxation.

## Acknowledgements

The authors sincerely thank the anonymous reviewers for their valuable and instructive comments and suggestions, which were very helpful for revising the manuscript. Also, we warmly thank Dr. Tao Chen (Southern University of Science and Technology), Dr. Yudong Zhang (Zhengzhou University), Dr. Chuandong Lin (Sun Yat-sen University), Dr. Dejia Zhang (China University of Mining and Technology (Beijing)), and Dr. Bohai Chen (North China Institute of Aerospace Engineering) for many helpful discussions. We acknowledge support from the National Natural Science Foundation of China (Grant Nos. 11875001 and 12172061), Natural Science Foundation of Hebei Province (Grant Nos. A2021409001 and 226Z7601G), “Three, Three and Three” Talent Project of Hebei Province (Grant No. A202105005), Natural Science Foundation of Fujian Province (Grant No. 2021J01652), CAEP Foundation (Grant No. CX2019033), the opening project of State Key Laboratory of Explosion Science and Technology (Beijing Institute of Technology) (Grant No. KFJJ21-16M) and Foundation of Laboratory of Computational Physics. SS gratefully acknowledges financial support from the European Research Council under the Horizon 2020 Programme Grant Agreement n. 739964 (“COPMAT”).

## Declaration of interests

The authors report no conflict of interest.

## Appendix A. Determination of the relations among THNE measures and TNE measures

According to the definitions in (2.9)-(2.10),  $\Delta_{m,n}$  describes the combination effects of thermodynamic non-equilibrium (TNE) and hydrodynamic non-equilibrium (HNE), which are usually called the thermo-hydrodynamic non-equilibrium (THNE) effects;  $\Delta_{m,n}^*$  reflects molecular individualism on top of organized collective motion, describing only the TNE effects. Next we give out the relations among them:

$$\begin{aligned}
 \Delta_2^* &= \mathbf{M}_2^*(f - f^{(0)}) = \int_{-\infty}^{\infty} (f - f^{(0)}) \mathbf{v}^* \mathbf{v}^* d\mathbf{v} & (A 1) \\
 &= \int_{-\infty}^{\infty} (f - f^{(0)}) (\mathbf{v} - \mathbf{u}) (\mathbf{v} - \mathbf{u}) d\mathbf{v} \\
 &= \int_{-\infty}^{\infty} (f - f^{(0)}) (\mathbf{v}\mathbf{v} - \mathbf{v}\mathbf{u} - \mathbf{u}\mathbf{v} + \mathbf{u}\mathbf{u}) d\mathbf{v} \\
 &= \Delta_2 + \int_{-\infty}^{\infty} (f - f^{(0)}) (-\mathbf{v}\mathbf{u}) d\mathbf{v} + \int_{-\infty}^{\infty} (f - f^{(0)}) (-\mathbf{u}\mathbf{v}) d\mathbf{v} + \int_{-\infty}^{\infty} (f - f^{(0)}) \mathbf{u}\mathbf{u} d\mathbf{v} \\
 &= \Delta_2 + \left[ \int_{-\infty}^{\infty} (f - f^{(0)}) (-\mathbf{v}) d\mathbf{v} \right] \mathbf{u} - \mathbf{u} \left[ \int_{-\infty}^{\infty} (f - f^{(0)}) \mathbf{v} d\mathbf{v} \right] + \left[ \int_{-\infty}^{\infty} (f - f^{(0)}) d\mathbf{v} \right] \mathbf{u}\mathbf{u}.
 \end{aligned}$$

It is well known that  $\int_{-\infty}^{\infty} (f - f^{(0)}) d\mathbf{v} = \mathbf{0}$  and  $\int_{-\infty}^{\infty} (f - f^{(0)}) \mathbf{v} d\mathbf{v} = \mathbf{0}$ , then

$$\Delta_2^* = \Delta_2. \quad (\text{A } 2)$$

$$\begin{aligned} \Delta_{3,1}^* &= \mathbf{M}_{3,1}^*(f - f^{(0)}) = \int_{-\infty}^{\infty} (f - f^{(0)}) \mathbf{v}^* \frac{\mathbf{v}^* \cdot \mathbf{v}^*}{2} d\mathbf{v} \\ &= \int_{-\infty}^{\infty} (f - f^{(0)}) (\mathbf{v} - \mathbf{u}) \frac{v^2 - 2\mathbf{v} \cdot \mathbf{u} + u^2}{2} d\mathbf{v} \\ &= \int_{-\infty}^{\infty} (f - f^{(0)}) \mathbf{v} \frac{v^2 - 2\mathbf{v} \cdot \mathbf{u} + u^2}{2} d\mathbf{v} - \int_{-\infty}^{\infty} (f - f^{(0)}) \mathbf{u} \frac{v^2 - 2\mathbf{v} \cdot \mathbf{u} + u^2}{2} d\mathbf{v}. \end{aligned} \quad (\text{A } 3)$$

It is clear that  $\int_{-\infty}^{\infty} (f - f^{(0)}) \frac{v^2}{2} d\mathbf{v} = \mathbf{0}$ , hence

$$\begin{aligned} \Delta_{3,1}^* &= \int_{-\infty}^{\infty} (f - f^{(0)}) \mathbf{v} \left( \frac{v^2}{2} - \mathbf{v} \cdot \mathbf{u} + \frac{u^2}{2} \right) d\mathbf{v} \\ &= \Delta_{3,1} + \int_{-\infty}^{\infty} (f - f^{(0)}) \mathbf{v} (-\mathbf{v} \cdot \mathbf{u} + \frac{u^2}{2}) d\mathbf{v} \\ &= \Delta_{3,1} - \left[ \int_{-\infty}^{\infty} (f - f^{(0)}) \mathbf{v} \mathbf{v} d\mathbf{v} \right] \cdot \mathbf{u} \\ &= \Delta_{3,1} - \Delta_2^* \cdot \mathbf{u}. \end{aligned} \quad (\text{A } 4)$$

Similarly,

$$\begin{aligned} \Delta_3^* &= \mathbf{M}_3^*(f - f^{(0)}) = \int_{-\infty}^{\infty} (f - f^{(0)}) \mathbf{v}^* \mathbf{v}^* \mathbf{v}^* d\mathbf{v} \\ &= \int_{-\infty}^{\infty} (f - f^{(0)}) (\mathbf{v} - \mathbf{u}) (\mathbf{v} - \mathbf{u}) (\mathbf{v} - \mathbf{u}) d\mathbf{v} \\ &= \int_{-\infty}^{\infty} (f - f^{(0)}) (\mathbf{v}\mathbf{v} - \mathbf{v}\mathbf{u} - \mathbf{u}\mathbf{v} + \mathbf{u}\mathbf{u}) (\mathbf{v} - \mathbf{u}) d\mathbf{v} \\ &= \int_{-\infty}^{\infty} (f - f^{(0)}) (\mathbf{v}\mathbf{v}\mathbf{v} - \mathbf{v}\mathbf{u}\mathbf{v} - \mathbf{u}\mathbf{v}\mathbf{v} + \mathbf{u}\mathbf{u}\mathbf{v} - \mathbf{v}\mathbf{v}\mathbf{u} + \mathbf{v}\mathbf{u}\mathbf{u} + \mathbf{u}\mathbf{v}\mathbf{u} - \mathbf{u}\mathbf{u}\mathbf{u}) d\mathbf{v} \\ &= \int_{-\infty}^{\infty} (f - f^{(0)}) (\mathbf{v}\mathbf{v}\mathbf{v} - \mathbf{v}\mathbf{u}\mathbf{v} - \mathbf{u}\mathbf{v}\mathbf{v} - \mathbf{v}\mathbf{v}\mathbf{u}) d\mathbf{v} \\ &= \Delta_3 - \int_{-\infty}^{\infty} (f - f^{(0)}) (\mathbf{v}\mathbf{u}\mathbf{v} + \mathbf{u}\mathbf{v}\mathbf{v} + \mathbf{v}\mathbf{v}\mathbf{u}) d\mathbf{v} \\ &= \Delta_3 - \int_{-\infty}^{\infty} (f - f^{(0)}) \mathbf{v}\mathbf{u}\mathbf{v} d\mathbf{v} - \mathbf{u}\Delta_2^* - \Delta_2^* \mathbf{u} \\ &= \Delta_3 - (u_\alpha \Delta_{2\beta\gamma}^* + u_\beta \Delta_{2\alpha\gamma}^* + u_\gamma \Delta_{2\alpha\beta}^*) \mathbf{e}_\alpha \mathbf{e}_\beta \mathbf{e}_\gamma, \end{aligned} \quad (\text{A } 5)$$

$$\begin{aligned} \Delta_{4,2}^* &= \mathbf{M}_{4,2}^*(f - f^{(0)}) = \int_{-\infty}^{\infty} (f - f^{(0)}) \mathbf{v}^* \mathbf{v}^* \frac{\mathbf{v}^* \cdot \mathbf{v}^*}{2} d\mathbf{v} \\ &= \int_{-\infty}^{\infty} (f - f^{(0)}) (\mathbf{v} - \mathbf{u}) (\mathbf{v} - \mathbf{u}) \left( \frac{v^2}{2} - \mathbf{v} \cdot \mathbf{u} + \frac{u^2}{2} \right) d\mathbf{v} \\ &= \int_{-\infty}^{\infty} (f - f^{(0)}) (\mathbf{v}\mathbf{v} - \mathbf{v}\mathbf{u} - \mathbf{u}\mathbf{v} + \mathbf{u}\mathbf{u}) \left( \frac{v^2}{2} - \mathbf{v} \cdot \mathbf{u} + \frac{u^2}{2} \right) d\mathbf{v} \end{aligned} \quad (\text{A } 6)$$

$$\begin{aligned}
&= \int_{-\infty}^{\infty} (f - f^{(0)}) (\mathbf{v}\mathbf{v} - \mathbf{v}\mathbf{u} - \mathbf{u}\mathbf{v}) \left( \frac{v^2}{2} - \mathbf{v} \cdot \mathbf{u} + \frac{u^2}{2} \right) d\mathbf{v} \\
&= \int_{-\infty}^{\infty} (f - f^{(0)}) \left( \mathbf{v}\mathbf{v} \frac{v^2}{2} - \mathbf{v}\mathbf{u} \frac{v^2}{2} - \mathbf{u}\mathbf{v} \frac{v^2}{2} \right) d\mathbf{v} \\
&\quad - \int_{-\infty}^{\infty} (f - f^{(0)}) (\mathbf{v}\mathbf{v}\mathbf{v} \cdot \mathbf{u} - \mathbf{v}\mathbf{u}\mathbf{v} \cdot \mathbf{u} - \mathbf{u}\mathbf{v}\mathbf{v} \cdot \mathbf{u}) d\mathbf{v} + \int_{-\infty}^{\infty} (f - f^{(0)}) \mathbf{v}\mathbf{v} \frac{u^2}{2} d\mathbf{v} \\
&= \mathbf{\Delta}_{4,2} - \mathbf{\Delta}_{3,1} \mathbf{u} - \mathbf{u} \mathbf{\Delta}_{3,1} - \mathbf{\Delta}_3 \cdot \mathbf{u} + \int_{-\infty}^{\infty} (f - f^{(0)}) (\mathbf{v}\mathbf{u}\mathbf{v} \cdot \mathbf{u}) d\mathbf{v} + \mathbf{u} \mathbf{\Delta}_2 \cdot \mathbf{u} + \frac{u^2}{2} \mathbf{\Delta}_2 \\
&= \mathbf{\Delta}_{4,2} - (\mathbf{\Delta}_{3,1}^* + \mathbf{\Delta}_2^* \cdot \mathbf{u}) \mathbf{u} - \mathbf{u} (\mathbf{\Delta}_{3,1}^* + \mathbf{\Delta}_2^* \cdot \mathbf{u}) \\
&\quad - (\mathbf{\Delta}_3^* + \int_{-\infty}^{\infty} (f - f^{(0)}) \mathbf{v}\mathbf{u}\mathbf{v} d\mathbf{v} + \mathbf{u} \mathbf{\Delta}_2^* + \mathbf{\Delta}_2^* \mathbf{u}) \cdot \mathbf{u} \\
&\quad + \int_{-\infty}^{\infty} (f - f^{(0)}) (\mathbf{v}\mathbf{u}\mathbf{v} \cdot \mathbf{u}) d\mathbf{v} + \mathbf{u} \mathbf{\Delta}_2 \cdot \mathbf{u} + \frac{u^2}{2} \mathbf{\Delta}_2 \\
&= \mathbf{\Delta}_{4,2} - \mathbf{\Delta}_{3,1}^* \mathbf{u} - \mathbf{u} \mathbf{\Delta}_{3,1}^* - \mathbf{\Delta}_3^* \cdot \mathbf{u} - \mathbf{\Delta}_2^* \cdot \mathbf{u} \mathbf{u} - \mathbf{u} \mathbf{\Delta}_2^* \cdot \mathbf{u} - \frac{u^2}{2} \mathbf{\Delta}_2^*.
\end{aligned}$$

According to the decomposition relations listed above, the formulas of THNE measures  $(\mathbf{\Delta}_2, \mathbf{\Delta}_{3,1}, \mathbf{\Delta}_3, \mathbf{\Delta}_{4,2})$  can be obtained only by knowing the expressions of TNE measures  $(\mathbf{\Delta}_2^*, \mathbf{\Delta}_{3,1}^*, \mathbf{\Delta}_3^*, \mathbf{\Delta}_{4,2}^*)$ .

---

**Appendix B. Expressions for the first- and second-order TNE measures**


---

$$\begin{aligned} \Delta_{2\alpha\beta}^{*(1)} & \Delta_{2xx}^{*(1)} = -\rho T \tau A_{1,-1} \\ & \Delta_{2xy}^{*(1)} = -\rho T \tau a_{1,1} \\ & \Delta_{2yy}^{*(1)} = -\Delta_{2xx}^{*(1)} \end{aligned}$$


---

$$\begin{aligned} \Delta_{3,1\alpha}^{*(1)} & \Delta_{3,1x}^{*(1)} = -2\rho T \tau \partial_x T \\ & \Delta_{3,1y}^{*(1)} = -2\rho T \tau \partial_y T \end{aligned}$$


---

$$\begin{aligned} \Delta_{3\alpha\beta\gamma}^{*(1)} & \Delta_{3xxx}^{*(1)} = -3\rho T \tau \partial_x T \\ & \Delta_{3xxy}^{*(1)} = -\rho T \tau \partial_y T \\ & \Delta_{3xyy}^{*(1)} = -\rho T \tau \partial_x T \\ & \Delta_{3yyy}^{*(1)} = -3\rho T \tau \partial_y T \end{aligned}$$


---

$$\begin{aligned} \Delta_{4,2\alpha\beta}^{*(1)} & \Delta_{4,2xx}^{*(1)} = -3\rho T^2 \tau A_{1,-1} \\ & \Delta_{4,2xy}^{*(1)} = -3\rho T^2 \tau a_{1,1} \\ & \Delta_{4,2yy}^{*(1)} = -\Delta_{4,2xx}^{*(1)} \end{aligned}$$


---

$$\begin{aligned} \Delta_{2xx}^{*2}/\tau^2 & = -(2C_1 A_{1,-1} + B_{1,-1}) \rho T^2 - [D_{1,-1} + \Gamma(u_x)_{1,-1} + \Gamma(u_y)_{1,-1}] \rho T \\ & \quad - T^2 F(\rho)_{1,-1} + \rho \Gamma(T)_{1,-1} + \frac{T^2}{\rho} \Gamma(\rho)_{1,-1} \\ \Delta_{2xy}^{*2}/\tau^2 & = -(2C_1 a_{1,1} + b_{1,1}) \rho T^2 - (d_{1,1} + 2E_{1,1}) \rho T - 2T^2 \lambda(\rho) + 2\rho \theta(T) + \frac{2T^2}{\rho} \theta(\rho) \\ \Delta_{2yy}^{*2} & = -\Delta_{2xx}^{*2} \end{aligned}$$


---

$$\begin{aligned} \Delta_{3,1x}^{*2}/\tau^2 & = -4\rho T^3 \partial_x C_1 - [A_{1,-1} B_x + a_{1,1} B_y + 12C_1 \partial_x T + F(u_x)_{1,-1} + 2\lambda(u_y)] \rho T^2 \\ & \quad + (A_{1,-3} \partial_x T + a_{1,3} \partial_y T) 2\rho T \\ \Delta_{3,1y}^{*2}/\tau^2 & = -4\rho T^3 \partial_y C_1 - [a_{1,1} B_x - A_{1,-1} B_y + 12C_1 \partial_y T - F(u_y)_{1,-1} + 2\lambda(u_x)] \rho T^2 \\ & \quad + (a_{3,1} \partial_x T + A_{-3,1} \partial_y T) 2\rho T \end{aligned}$$


---

$$\begin{aligned} \Delta_{3xxx}^{*2}/\tau^2 & = -6\rho T^3 \partial_x C_1 - [A_{1,-1} B_x + 6C_1 \partial_x T + 2\lambda(u_y)] 3\rho T^2 + (A_{1,-2} \partial_x T + \partial_y u_x \partial_y T) 6\rho T \\ \Delta_{3yyy}^{*2}/\tau^2 & = -6\rho T^3 \partial_y C_1 - [A_{-1,1} B_y + 6C_1 \partial_y T + 2\lambda(u_x)] 3\rho T^2 + (A_{-2,1} \partial_y T + \partial_x u_y \partial_x T) 6\rho T \\ \Delta_{3xy}^{*(2)} & = 2\Delta_{3,1y}^{*(2)} - \Delta_{3yyy}^{*(2)} \\ \Delta_{3yx}^{*(2)} & = 2\Delta_{3,1x}^{*(2)} - \Delta_{3xxx}^{*(2)} \end{aligned}$$


---

$$\begin{aligned} \Delta_{4,2xx}^{*2}/\tau^2 & = -(4C_1 A_{1,-1} + B_{1,-1}) 3\rho T^3 \\ & \quad - [D_{10,-2} + \Gamma(u_x)_{1,-5} + \Gamma(u_y)_{1,-5} + 4e_{1,-1} - F(T)_{7,1}] \rho T^2 \\ & \quad + 3\rho T \Gamma(T)_{7,1} - 3T^3 F(\rho)_{1,-1} + \frac{3T^3}{\rho} \Gamma(\rho)_{1,-1} \\ \Delta_{4,2xy}^{*2}/\tau^2 & = -(4C_1 a_{11} + b_{1,1}) 3\rho T^3 - [d_{1,1} + E_{1,1} - \lambda(T)] 6\rho T^2 \\ & \quad + 18\rho T \theta(T) - 6T^3 \lambda(\rho) + \frac{6T^3}{\rho} \theta(\rho) \\ \Delta_{4,2yy}^{*2}/\tau^2 & = (4C_1 A_{1,-1} + B_{1,-1}) 3\rho T^3 \\ & \quad + [D_{2,-10} + \Gamma(u_x)_{5,-1} + \Gamma(u_y)_{5,-1} + 4e_{-1,1} + F(T)_{1,7}] \rho T^2 \\ & \quad + 3\rho T \Gamma(T)_{1,7} + 3T^3 F(\rho)_{1,-1} - \frac{3T^3}{\rho} \Gamma(\rho)_{1,-1}, \end{aligned}$$


---



where  $A_{m,n} = m\partial_x u_x + n\partial_y u_y$ ,  $a_{m,n} = m\partial_x u_y + m\partial_y u_x$ ,  $B_{m,n} = m\partial_x B_x + n\partial_y B_y$ ,  
 $b_{m,n} = m\partial_x B_y + n\partial_y B_x$ ,  $D_{m,n} = mB_x\partial_x T + nB_y\partial_y T$ ,  $d_{m,n} = mB_y\partial_x T + nB_x\partial_y T$ ,  
 $E_{m,n} = m\partial_x u_x\partial_y u_x + n\partial_x u_y\partial_y u_y$ ,  $e_{m,n} = m\partial_x u_x\partial_y u_y + n\partial_x u_y\partial_y u_x$ ,  $\theta(\cdot) = \partial_x(\cdot)\partial_y(\cdot)$ ,  
 $\lambda(\cdot) = \frac{\partial^2}{\partial y\partial x}(\cdot)$ ,  $F(\cdot)_{m,n} = m\frac{\partial^2}{\partial x^2}(\cdot) + n\frac{\partial^2}{\partial y^2}(\cdot)$ ,  $\Gamma(\cdot)_{m,n} = m[\partial_x(\cdot)]^2 + n[\partial_y(\cdot)]^2$ ,  $C_1 = C + C_q$ .

---

**Appendix C. Independent kinetic moments required for fully characterize the first- and second-order TNE measures**

$\mathbf{M}_m$	Independent kinetic moments
$\mathbf{M}_0$	$M_0 = \rho$
$\mathbf{M}_1$	$M_{1x} = \rho u_x$ $M_{1y} = \rho u_y$
$\mathbf{M}_2$	$M_{2xx} = \rho(T + u_x^2)$ $M_{2xy} = \rho u_x u_y$ $M_{2yy} = \rho(T + u_y^2)$
$\mathbf{M}_3$	$M_{3xxx} = \rho u_x(3T + u_x^2)$ $M_{3xxy} = \rho u_y(T + u_x^2)$ $M_{3xyy} = \rho u_x(T + u_y^2)$ $M_{3yyy} = \rho u_y(3T + u_y^2)$
$\mathbf{M}_4$	$M_{4xxxx} = \rho(3T^2 + 6T u_x^2 + u_x^4)$ $M_{4xxxxy} = \rho u_x u_y(3T + u_x^2)$ $M_{4xxyy} = \rho(T + u_x^2)(T + u_y^2)$ $M_{4xyyy} = \rho u_x u_y(3T + u_y^2)$ $M_{4yyyy} = \rho(3T^2 + 6T u_y^2 + u_y^4)$
$\mathbf{M}_5$	$M_{5xxxxx} = \rho u_x(15T^2 + 10T u_x^2 + u_x^4)$ $M_{5xxxxy} = \rho u_y(3T^2 + 6T u_x^2 + u_x^4)$ $M_{5xxxxy} = \rho u_x(3T + u_x^2)(T + u_y^2)$ $M_{5xxyyy} = \rho u_y(3T + u_y^2)(T + u_x^2)$ $M_{5xyyyy} = \rho u_x(3T^2 + 6T u_y^2 + u_y^4)$ $M_{5yyyyy} = \rho u_y(15T^2 + 10T u_y^2 + u_y^4)$
$\mathbf{M}_{6,4}$	$M_{6,4xxxx} = \frac{1}{2}\rho[18T^3 + 3T^2(u^2 + 16u_x^2) + 2T u_x^2(3u^2 + 5u_x^2) + u^2 u_x^4]$ $M_{6,4xxxxy} = \frac{1}{2}\rho u_x u_y[24T^2 + T(3u^2 + 10u_x^2) + u^2 u_x^2]$ $M_{6,4xxyy} = \frac{1}{2}\rho[6T^3 + T u^2(9T + u^2) + u_x^2 u_y^2(10T + u^2)]$ $M_{6,4xyyy} = \frac{1}{2}\rho u_x u_y[24T^2 + T(3u^2 + 10u_y^2) + u^2 u_y^2]$ $M_{6,4yyyy} = \frac{1}{2}\rho[18T^3 + 3T^2(u^2 + 16u_y^2) + 2T u_y^2(3u^2 + 5u_y^2) + u^2 u_y^4]$
$\mathbf{M}_{7,3}$	$M_{7,3xxx} = \frac{1}{2}\rho u_x[144T^3 + 16T^2(3u^2 + 5u_x^2) + T u^2(3u^2 + 20u_x^2) + u^4 u_x^2]$ $M_{7,3xxy} = \frac{1}{2}\rho u_y[48T^3 + 16T^2(u^2 + 5u_x^2) + T u^2(u^2 + 20u_x^2) + u^4 u_x^2]$ $M_{7,3xyy} = \frac{1}{2}\rho u_x[48T^3 + 16T^2(u^2 + 5u_y^2) + T u^2(u^2 + 20u_y^2) + u^4 u_y^2]$ $M_{7,3yyy} = \frac{1}{2}\rho u_y[144T^3 + 16T^2(3u^2 + 5u_y^2) + T u^2(3u^2 + 20u_y^2) + u^4 u_y^2]$

---

## REFERENCES

- AARTS, D. G. A. L., SCHMIDT, M. & LEKKERKERKER, H. N. W. 2004 Direct visual observation of thermal capillary waves. *Science* **304** (5672), 847–850.
- AMBRUŞ, V. E., BUSUIOC, S., WAGNER, A. J., PAILLUSSON, F. & KUSUMAATMAJA, H. 2019 Multicomponent flow on curved surfaces: A vielbein lattice Boltzmann approach. *Phys. Rev. E* **100** (6), 063306.
- AMBRUŞ, V. E. & SOFONEA, V. 2016 Lattice Boltzmann models based on half-range Gauss-Hermite quadratures. *J. Comput. Phys.* **316**, 760–788.
- ANSUMALI, S., KARLIN, I. V., ARCIDIACONO, S., ABBAS, A. & PRASIANAKIS, N. I. 2007 Hydrodynamics beyond Navier-Stokes: Exact solution to the lattice Boltzmann hierarchy. *Phys. Rev. Lett.* **98** (12), 124502.
- BAO, Y., QIU, R., ZHOU, K., ZHOU, T., WENG, Y., LIN, K. & YOU, Y. 2022 Study of shock wave/boundary layer interaction from the perspective of nonequilibrium effects. *Phys. Fluids* **34** (4), 046109.
- BEDAUX, D. 1986 Nonequilibrium thermodynamics and statistical physics of surfaces. *Adv. Chem. Phys.* **64**, 47–109.
- BENZI, R., BIFERALE, L., SBRAGAGLIA, M., SUCCI, S. & TOSCHI, F. 2006 Mesoscopic two-phase model for describing apparent slip in micro-channel flows. *EPL* **74** (4), 651.
- BENZI, R., SUCCI, S. & VERGASSOLA, M. 1992 The lattice Boltzmann equation: theory and applications. *Phys. Rep.* **222** (3), 145–197.
- BERNASCHI, M., MELCHIONNA, S. & SUCCI, S. 2019 Mesoscopic simulations at the physics-chemistry-biology interface. *Rev. Mod. Phys.* **91** (2), 025004.
- BHAIRAPURADA, K., DENET, B. & BOIVIN, P. 2022 A lattice-Boltzmann study of premixed flames thermo-acoustic instabilities. *Combust. Flame* **240**, 112049.
- BHATNAGAR, P. L., GROSS, E. P. & KROOK, M. 1954 A model for collision processes in gases. I. Small amplitude processes in charged and neutral one-component systems. *Phys. Rev.* **94** (3), 511.
- BIFERALE, L., PERLEKAR, P., SBRAGAGLIA, M. & TOSCHI, F. 2012 Convection in multiphase fluid flows using lattice Boltzmann methods. *Phys. Rev. Lett.* **108** (10), 104502.
- BRENNEN, C. E. 2005 *Fundamentals of Multiphase Flow*. Cambridge University Press.
- BU, W., KIM, D. & VAKNIN, D. 2014 Density profiles of liquid/vapor interfaces away from their critical points. *J. Phys. Chem. C* **118** (23), 12405–12409.
- BUSUIOC, S., AMBRUŞ, V. E., BICIUŞCĂ, T. & SOFONEA, V. 2020 Two-dimensional off-lattice Boltzmann model for van der Waals fluids with variable temperature. *Comput. Math. Appl.* **79** (1), 111–140.
- CARENZA, L. N., GONNELLA, G., MARENDUZZO, D. & NEGRO, G. 2019 Rotation and propulsion in 3D active chiral droplets. *Proc. Natl. Acad. Sci.* **116** (44), 22065–22070.
- CARNAHAN, N. F. & STARLING, K. E. 1969 Equation of state for nonattracting rigid spheres. *J. Chem. Phys.* **51** (2), 635–636.
- CATES, M. E., FIELDING, S. M., MARENDUZZO, D., ORLANDINI, E. & YEOMANS, J. M. 2008 Shearing active gels close to the isotropic-nematic transition. *Phys. Rev. Lett.* **101** (6), 068102.
- CHAI, Z., HUANG, C., SHI, B. & GUO, Z. 2016 A comparative study on the lattice Boltzmann models for predicting effective diffusivity of porous media. *Int. J. Heat Mass Transfer* **98**, 687–696.

- CHAI, Z., LIANG, H., DU, R. & SHI, B. 2019 A lattice Boltzmann model for two-phase flow in porous media. *SIAM J. Sci. Comput.* **41** (4), B746–B772.
- CHAI, Z. & SHI, B. 2008 A novel lattice Boltzmann model for the Poisson equation. *App. Math. Model.* **32** (10), 2050–2058.
- CHAPMAN, S. & COWLING, T. G. 1990 *The mathematical theory of non-uniform gases: an account of the kinetic theory of viscosity, thermal conduction and diffusion in gases.* Cambridge University Press.
- CHEN, F., XU, A., ZHANG, Y., GAN, Y., LIU, B. & WANG, S. 2022a Delineation of the flow and mixing induced by Rayleigh-Taylor instability through tracers. *Front. Phys.* **17** (3), 33505.
- CHEN, F., XU, A., ZHANG, Y. & ZENG, Q. 2020 Morphological and non-equilibrium analysis of coupled Rayleigh-Taylor-Kelvin-Helmholtz instability. *Phys. Fluids* **32** (10), 104111.
- CHEN, L., KANG, Q., TANG, Q., ROBINSON, B. A., HE, Y. & TAO, W. 2015 Pore-scale simulation of multicomponent multiphase reactive transport with dissolution and precipitation. *Int. J. Heat Mass Transfer* **85**, 935–949.
- CHEN, L., KANG, Q. & TAO, W. 2021a Pore-scale numerical study of multiphase reactive transport processes in cathode catalyst layers of proton exchange membrane fuel cells. *Int. J. Hydrogen Energy* **46** (24), 13283–13297.
- CHEN, Q., ZHANG, X. & ZHANG, J. 2013 Improved treatments for general boundary conditions in the lattice Boltzmann method for convection-diffusion and heat transfer processes. *Phys. Rev. E* **88** (3), 033304.
- CHEN, S. & DOOLEN, G. D. 1998 Lattice Boltzmann method for fluid flows. *Annual review of fluid mechanics* **30** (1), 329–364.
- CHEN, T., WU, L., WANG, L. & CHEN, S. 2022b Rarefaction effects in head-on collision of two identical droplets. *arXiv preprint arXiv:2205.03604* .
- CHEN, X., CHAI, Z., SHANG, J. & SHI, B. 2021b Multiple-relaxation-time finite-difference lattice Boltzmann model for the nonlinear convection-diffusion equation. *Phys. Rev. E* **104** (3), 035308.
- CHEN, X., ZHONG, C. & YUAN, X. 2011 Lattice Boltzmann simulation of cavitating bubble growth with large density ratio. *Comput. Math. Appl.* **61** (12), 3577–3584.
- CHEN, Y. & DENG, Z. 2017 Hydrodynamics of a droplet passing through a microfluidic T-junction. *J. Fluid Mech.* **819**, 401–434.
- CHEN, Z., SHU, C., YANG, L. M., ZHAO, X. & LIU, N. Y. 2021c Phase-field-simplified lattice Boltzmann method for modeling solid-liquid phase change. *Phys. Rev. E* **103** (2), 023308.
- CHIKATAMARLA, S. S., ANSUMALI, S. & KARLIN, I. V. 2006 Grad’s approximation for missing data in lattice Boltzmann simulations. *EPL* **74** (2), 215.
- CHIKATAMARLA, S. S. & KARLIN, I. V. 2009 Lattices for the lattice Boltzmann method. *Phys. Rev. E* **79** (4), 046701.
- COCLITE, A., GONNELLA, G. & LAMURA, A. 2014 Pattern formation in liquid-vapor systems under periodic potential and shear. *Phys. Rev. E* **89** (6), 063303.
- CORBERI, F., GONNELLA, G. & LAMURA, A. 1998 Spinodal decomposition of binary mixtures in uniform shear flow. *Phys. Rev. Lett.* **81** (18), 3852.
- COREIXAS, C., WISSOCQ, G., PUIGT, G., BOUSSUGE, J. & SAGAUT, P. 2017 Recursive regularization step for high-order lattice Boltzmann methods. *Phys. Rev. E* **96** (3), 033306.
- CZELUSNIAK, L. E., MAPELLI, V. P., GUZELLA, M. S., CABEZAS-GÓMEZ, L. & WAGNER,

- A. J. 2020 Force approach for the pseudopotential lattice Boltzmann method. *Phys. Rev. E* **102** (3), 033307.
- DAI, R., LI, W., MOSTAGHIMI, J., WANG, Q. & ZENG, M. 2020 On the optimal heat source location of partially heated energy storage process using the newly developed simplified enthalpy based lattice Boltzmann method. *Appl. Energy* **275**, 115387.
- DOOSTMOHAMMADI, A., ADAMER, M. F., THAMPI, S. P. & YEOMANS, J. M. 2016 Stabilization of active matter by flow-vortex lattices and defect ordering. *Nat. Commun.* **7** (1), 1–9.
- DU, R. & LIU, Z. 2020 A lattice Boltzmann model for the fractional advection-diffusion equation coupled with incompressible Navier-Stokes equation. *Appl. Math. Lett.* **101**, 106074.
- DUAN, Y. & LIU, R. 2007 Lattice Boltzmann model for two-dimensional unsteady Burgers' equation. *J. Comput. Appl. Math.* **206** (1), 432–439.
- DUPIN, M., HALLIDAY, I. & CARE, C. 2006 A multi-component lattice Boltzmann scheme: towards the mesoscale simulation of blood flow. *Med. Eng. Phys.* **28** (1), 13–18.
- ELTON, B. H. 1996 Comparisons of lattice Boltzmann and finite difference methods for a two-dimensional viscous Burgers equation. *SIAM J. Sci. Comput.* **17** (4), 783–813.
- EVANS, R. 1979 The nature of the liquid-vapour interface and other topics in the statistical mechanics of non-uniform, classical fluids. *Adv. Phys.* **28** (2), 143–200.
- FAKHARI, A. & LEE, T. 2013 Multiple-relaxation-time lattice Boltzmann method for immiscible fluids at high Reynolds numbers. *Phys. Rev. E* **87** (2), 023304.
- FALCUCCI, G., AMATI, G., FANELLI, P., KRASSTEV, V. K., POLVERINO, G., PORFIRI, M. & SUCCI, S. 2021 Extreme flow simulations reveal skeletal adaptations of deep-sea sponges. *Nature* **595** (7868), 537–541.
- FALCUCCI, G., CHIATTI, G., SUCCI, S., MOHAMAD, A. A. & KUZMIN, A. 2009 Rupture of a ferrofluid droplet in external magnetic fields using a single-component lattice Boltzmann model for nonideal fluids. *Phys. Rev. E* **79** (5), 056706.
- FALCUCCI, G., JANNELLI, E., UBERTINI, S. & SUCCI, S. 2013 Direct numerical evidence of stress-induced cavitation. *J. Fluid Mech.* **728**, 362–375.
- FEI, L., YANG, J., CHEN, Y., MO, H. & LUO, K. H. 2020 Mesoscopic simulation of three-dimensional pool boiling based on a phase-change cascaded lattice Boltzmann method. *Phys. Fluids* **32** (10), 103312.
- FREZZOTTI, A. 2011 Boundary conditions at the vapor-liquid interface. *Phys. fluids* **23** (3), 030609.
- FREZZOTTI, A., BARBANTE, P. & GIBELLI, L. 2019 Direct simulation Monte Carlo applications to liquid-vapor flows. *Phys. Fluids* **31** (6), 062103.
- FREZZOTTI, A., GIBELLI, L., LOCKERBY, D. A. & SPRITTLES, J. E. 2018 Mean-field kinetic theory approach to evaporation of a binary liquid into vacuum. *Phys. Rev. Fluids* **3** (5), 054001.
- FREZZOTTI, A., GIBELLI, L. & LORENZANI, S. 2005 Mean field kinetic theory description of evaporation of a fluid into vacuum. *Phys. Fluids* **17** (1), 012102.
- FREZZOTTI, A. & ROSSI, M. 2012 Slip effects at the vapor-liquid boundary. *AIP Conf. Proc.* **1501** (1), 903–910.
- GAN, Y., XU, A., ZHANG, G. & LI, Y. 2012a Physical modeling of multiphase flow via lattice Boltzmann method: Numerical effects, equation of state and boundary conditions. *Front. Phys.* **7** (4), 481–490.
- GAN, Y., XU, A., ZHANG, G., LI, Y. & LI, H. 2011 Phase separation in thermal systems: A lattice Boltzmann study and morphological characterization. *Phys. Rev. E* **84** (4), 046715.

- GAN, Y., XU, A., ZHANG, G. & SUCCI, S. 2015 Discrete Boltzmann modeling of multiphase flows: hydrodynamic and thermodynamic non-equilibrium effects. *Soft Matter* **11** (26), 5336–5345.
- GAN, Y., XU, A., ZHANG, G. & YANG, Y. 2013 Lattice bgk kinetic model for high speed compressible flows: hydrodynamic and nonequilibrium behaviors. *EPL* **103** (2), 24003.
- GAN, Y., XU, A., ZHANG, G., YU, X. & LI, Y. 2008 Two-dimensional lattice Boltzmann model for compressible flows with high mach number. *Physica A* **387** (8-9), 1721–1732.
- GAN, Y., XU, A., ZHANG, G., ZHANG, P. & LI, Y. 2012*b* Lattice Boltzmann study of thermal phase separation: Effects of heat conduction, viscosity and Prandtl number. *EPL* **97** (4), 44002.
- GAN, Y., XU, A., ZHANG, G., ZHANG, Y. & SUCCI, S. 2018 Discrete Boltzmann trans-scale modeling of high-speed compressible flows. *Phys. Rev. E* **97** (5), 053312.
- GAN, Y. B., XU, A. G., ZHANG, G. C., LIN, C. D. & LIU, Z. P. 2019 Nonequilibrium and morphological characterizations of kelvin-Helmholtz instability in compressible flows. *Front. Phys.* **14** (4), 43602.
- GAO, W. & SUN, Q. 2014 Evaluation of BGK-type models of the Boltzmann equation **1628** (1), 84–91.
- GONNELLA, G., LAMURA, A., PISCITELLI, A. & TIRIBOCCHI, A. 2010 Phase separation of binary fluids with dynamic temperature. *Phys. Rev. E* **82** (4), 046302.
- GONNELLA, G., LAMURA, A. & SOFONEA, V. 2007 Lattice Boltzmann simulation of thermal nonideal fluids. *Phys. Rev. E* **76** (3), 036703.
- GONNELLA, G., ORLANDINI, E. & YEOMANS, J. M. 1997 Spinodal decomposition to a lamellar phase: effects of hydrodynamic flow. *Phys. Rev. Lett.* **78** (9), 1695.
- GUNSTENSEN, A. K., ROTHMAN, D. H., ZALESKI, S. & ZANETTI, G. 1991 Lattice Boltzmann model of immiscible fluids. *Phys. Rev. A* **43** (8), 4320–4327.
- GUO, Z. & SHU, C. 2013 *Lattice Boltzmann Method and Its Applications in Engineering*. World Scientific Publishing.
- GUO, Z., WANG, R. & XU, K. 2015 Discrete unified gas kinetic scheme for all Knudsen number flows. II. Thermal compressible case. *Phys. Rev. E* **91** (3), 033313.
- GURTIN, M. E. & VOORHEES, P. W. 1996 The thermodynamics of evolving interfaces far from equilibrium. *Acta Mater.* **44** (1), 235–247.
- HE, B., QIN, C., CHEN, W. & WEN, B. 2022 Numerical simulation of pulmonary airway reopening by the multiphase lattice Boltzmann method. *Comput. Math. Appl.* **108**, 196–205.
- HE, X., CHEN, S. & ZHANG, R. 1999*a* A lattice Boltzmann scheme for incompressible multiphase flow and its application in simulation of Rayleigh-Taylor instability. *J. Comput. Phys.* **152** (2), 642–663.
- HE, X., SHAN, X. & DOOLEN, G. D. 1998 Discrete Boltzmann equation model for nonideal gases. *Phys. Rev. E* **57** (1), R13–R16.
- HE, X., ZHANG, R., CHEN, S. & DOOLEN, G. D. 1999*b* On the three-dimensional Rayleigh-Taylor instability. *Phys. Fluids* **11** (5), 1143–1152.
- HE, Y. & LIN, X. 2020 Numerical analysis and simulations for coupled nonlinear Schrödinger equations based on lattice Boltzmann method. *Appl. Math. Lett.* **106**, 106391.
- HE, Y., LIU, Q., LI, Q. & TAO, W. 2019 Lattice Boltzmann methods for single-phase and solid-liquid phase-change heat transfer in porous media: A review. *Int. J. Heat Mass Transfer* **129**, 160–197.

- HOLWAY JR., L. H. 1966 New statistical models for kinetic theory: methods of construction. *Phys. Fluids* **9** (9), 1658–1673.
- HU, Y., LI, D. & NIU, X. 2018 Phase-field-based lattice Boltzmann model for multiphase ferrofluid flows. *Phys. Rev. E* **98** (3), 033301.
- HUANG, Q., TIAN, F. B., YOUNG, J. & LAI, J. C. S. 2021a Transition to chaos in a two-sided collapsible channel flow. *J. Fluid Mech.* **926**.
- HUANG, R., WU, H. & ADAMS, N. A. 2021b Mesoscopic lattice Boltzmann modeling of the liquid-vapor phase transition. *Phys. Rev. Lett.* **126** (24), 244501.
- JAENSSON, N. & VERMANT, J. 2018 Tensiometry and rheology of complex interfaces. *Curr. Opin. Colloid Interface Sci.* **37**, 136–150.
- KÄHLER, G., BONELLI, F., GONNELLA, G. & LAMURA, A. 2015 Cavitation inception of a van der Waals fluid at a sack-wall obstacle. *Phys. Fluids* **27** (12), 123307.
- KENDON, V. M., DESPLAT, J. C., BLADON, P. & CATES, M. E. 1999 3d spinodal decomposition in the inertial regime. *Phys. Rev. Lett.* **83** (3), 576.
- LAI, H. & MA, C. 2009 Lattice Boltzmann method for the generalized Kuramoto-Sivashinsky equation. *Physica A* **388** (8), 1405–1412.
- LAI, H. & MA, C. 2010 The lattice Boltzmann model for the second-order benjamin-ono equations. *J. Stat. Mech: Theory Exp.* **2010** (4), P04011.
- LAI, H. & MA, C. 2011 Lattice Boltzmann model for generalized nonlinear wave equations. *Phys. Rev. E* **84** (4), 046708.
- LAI, H., XU, A., ZHANG, G., GAN, Y., YING, Y. & SUCCI, S. 2016 Non-equilibrium thermodynamic effects on the Rayleigh-Taylor instability in compressible flows. *Phys. Rev. E* **94** (2), 023106.
- LAN, Z. Z., HU, W. Q. & GUO, B. L. 2019 General propagation lattice Boltzmann model for a variable-coefficient compound KdV-Burgers equation. *App. Math. Model.* **73**, 695–714.
- LANG, F. & LEIDERER, P. 2006 Liquid-vapour phase transitions at interfaces: sub-nanosecond investigations by monitoring the ejection of thin liquid films. *New J. Phys.* **8** (1), 14.
- LEDESMA-AGUILAR, R., VELLA, D. & YEOMANS, J. M. 2014 Lattice-Boltzmann simulations of droplet evaporation. *Soft Matter* **10** (41), 8267.
- LI, Q., LUO, K. H., KANG, Q. J., HE, Y. L., CHEN, Q. & LIU, Q. 2016 Lattice Boltzmann methods for multiphase flow and phase-change heat transfer. *Prog. Energy Combust. Sci.* **52**, 62–105.
- LI, Q., YU, Y., ZHOU, P. & YAN, H. J. 2018 Enhancement of boiling heat transfer using hydrophilic-hydrophobic mixed surfaces: A lattice Boltzmann study. *Appl. Therm. Eng.* **132**, 490–499.
- LI, W., LI, Q., YU, Y. & WEN, Z. 2020 Enhancement of nucleate boiling by combining the effects of surface structure and mixed wettability: A lattice Boltzmann study. *Appl. Therm. Eng.* **180**, 115849.
- LI, X., SHI, Y. & SHAN, X. 2019 Temperature-scaled collision process for the high-order lattice Boltzmann model. *Phys. Rev. E* **100** (1), 013301.
- LI, Z. H., PENG, A. P., ZHANG, H. X. & YANG, J. Y. 2015 Rarefied gas flow simulations using high-order gas-kinetic unified algorithms for Boltzmann model equations. *Prog. Aerosp. Sci.* **74**, 81–113.
- LI, Z. H. & ZHANG, H. X. 2004 Study on gas kinetic unified algorithm for flows from rarefied transition to continuum. *J. Comput. Phys.* **193** (2), 708–738.

- LIANG, H., LI, Q. X., SHI, B. C. & CHAI, Z. H. 2016a Lattice Boltzmann simulation of three-dimensional Rayleigh-Taylor instability. *Phys. Rev. E* **93** (3), 033113.
- LIANG, H., LI, Y., CHEN, J. & XU, J. 2019 Axisymmetric lattice Boltzmann model for multiphase flows with large density ratio. *Int. J. Heat Mass Transfer* **130**, 1189–1205.
- LIANG, H., SHI, B. C. & CHAI, Z. H. 2016b Lattice Boltzmann modeling of three-phase incompressible flows. *Phys. Rev. E* **93** (1), 013308.
- LIANG, H., SHI, B. C., GUO, Z. L. & CHAI, Z. H. 2014 Phase-field-based multiple-relaxation-time lattice Boltzmann model for incompressible multiphase flows. *Phys. Rev. E* **89** (5), 053320.
- LIN, C., LUO, K. H., FEI, L. & SUCCI, S. 2017 A multi-component discrete Boltzmann model for nonequilibrium reactive flows. *Sci. Rep.* **7** (1), 1–12.
- LIN, C., LUO, K. H., XU, A., GAN, Y. & LAI, H. 2021 Multiple-relaxation-time discrete Boltzmann modeling of multicomponent mixture with nonequilibrium effects. *Phys. Rev. E* **103** (1), 013305.
- LIN, C., XU, A., ZHANG, G. & LI, Y. 2016 Double-distribution-function discrete Boltzmann model for combustion. *Combust. Flame* **164**, 137–151.
- LIN, C., XU, A., ZHANG, G., LI, Y. & SUCCI, S. 2014 Polar coordinate lattice Boltzmann modeling of compressible flows. *Phys. Rev. E* **89** (1), 013307.
- LIU, F. & SHI, W. 2011 Numerical solutions of two-dimensional Burgers’s equations by lattice Boltzmann method. *Commun. Nonlinear Sci. Numer. Simul.* **16** (1), 150–157.
- LIU, H., BA, Y., WU, L., LI, Z., XI, G. & ZHANG, Y. 2018 A hybrid lattice Boltzmann and finite difference method for droplet dynamics with insoluble surfactants. *J. Fluid Mech.* **837**, 381–412.
- LIU, H., KANG, Q., LEONARDI, C. R., SCHMIESCHEK, S., NARVÁEZ, A., JONES, B. D., WILLIAMS, J. R., VALOCCHI, A. J. & HARTING, J. 2016 Multiphase lattice Boltzmann simulations for porous media applications. *Comput. Geosci.* **20** (4), 777–805.
- LIU, H., ZHANG, Y., KANG, W., ZHANG, P., DUAN, H. & HE, X. T. 2017 Molecular dynamics simulation of strong shock waves propagating in dense deuterium, taking into consideration effects of excited electrons. *Phys. Rev. E* **95** (2), 023201.
- LIU, H., ZHOU, H., KANG, W., ZHANG, P., DUAN, H., ZHANG, W. & HE, X. T. 2020 Dynamics of bond breaking and formation in polyethylene near shock front. *Phys. Rev. E* **102** (2), 023207.
- LIU, X., CHAI, Z. & SHI, B. 2019 A phase-field-based lattice Boltzmann modeling of two-phase electro-hydrodynamic flows. *Phys. Fluids* **31** (9), 092103.
- LIU, Z., SONG, J., XU, A., ZHANG, Y. & XIE, K. 2022 Discrete boltzmann modeling of plasma shock wave. *Proc. Inst. Mech. Eng. Part C J. Mech. Eng. Sci.* p. 09544062221075943.
- LUO, KAI H, FEI, LINLIN & WANG, GENG 2021 A unified lattice Boltzmann model and application to multiphase flows. *Phil. Trans. R. Soc. A.* **379** (2208), 20200397.
- LUO, K. H., XIA, J. & MONACO, E. 2009 Multiscale modeling of multiphase flow with complex interactions. *J. Multiscale Model.* **1** (1), 125–156.
- MAZLOOMI M, A., CHIKATAMARLA, S. S. & KARLIN, I. V. 2015 Entropic lattice Boltzmann method for multiphase flows. *Phys. Rev. Lett.* **114** (17), 174502.
- MENG, J. & ZHANG, Y. 2011 Accuracy analysis of high-order lattice Boltzmann models for rarefied gas flows. *J. Comput. Phys.* **230** (3), 835–849.
- MENG, J., ZHANG, Y., HADJICONSTANTINO, N. G., RADTKE, G. A. & SHAN, X. 2013 Lattice



- ellipsoidal statistical BGK model for thermal non-equilibrium flows. *J. Fluid Mech.* **718**, 347–370.
- MILAN, F., BIFERALE, L., SBRAGAGLIA, M. & TOSCHI, F. 2020 Sub-kolmogorov droplet dynamics in isotropic turbulence using a multiscale lattice Boltzmann scheme. *J. Comput. Sci.* **45**, 101178.
- MONTESSORI, A., PRESTININZI, P., LA ROCCA, M. & SUCCI, S. 2015 Lattice Boltzmann approach for complex nonequilibrium flows. *Phys. Rev. E* **92** (4), 043308.
- MONTESSORI, A., PRESTININZI, P., LA ROCCA, M. & SUCCI, S. 2017 Entropic lattice pseudopotentials for multiphase flow simulations at high Weber and Reynolds numbers. *Phys. Fluids* **29** (9), 092103.
- MYONG, R. S. 1999 Thermodynamically consistent hydrodynamic computational models for high-Knudsen-number gas flows. *Phys. Fluids* **11** (9), 2788–2802.
- NEGRO, G., CARENZA, L. N., LAMURA, A., TIRIBOCCHI, A. & GONNELLA, G. 2019 Rheology of active polar emulsions: from linear to unidirectional and inviscid flow, and intermittent viscosity. *Soft matter* **15** (41), 8251–8265.
- ONUKI, A. 2002 *Phase transition dynamics*. Cambridge University Press.
- ONUKI, A. 2005 Dynamic van der Waals theory of two-phase fluids in heat flow. *Phys. Rev. Lett.* **94** (5), 054501.
- ONUKI, A. 2007 Dynamic van der Waals theory. *Phys. Rev. E* **75** (3), 036304.
- OSBORN, W. R., ORLANDINI, E., SWIFT, M. R., YEOMANS, J. M. & BANAVAR, J. R. 1995 Lattice Boltzmann study of hydrodynamic spinodal decomposition. *Phys. Rev. Lett.* **75** (22), 4031.
- OTOMO, H., BOGHOSIAN, B. M. & DUBOIS, F. 2018 Efficient lattice Boltzmann models for the Kuramoto-Sivashinsky equation. *Comput. Fluids* **172**, 683–688.
- PACHALIEVA, A. & WAGNER, A. J. 2021 Connecting lattice Boltzmann methods to physical reality by coarse-graining Molecular Dynamics simulations. *arXiv preprint arXiv:2109.05009* .
- PARSA, M. R., KIM, C. & WAGNER, A. J. 2021 Nonuniqueness of fluctuating momentum in coarse-grained systems. *Phys. Rev. E* **104** (1), 015304.
- PARSA, M. R. & WAGNER, A. J. 2017 Lattice gas with molecular dynamics collision operator. *Phys. Rev. E* **96** (1), 013314.
- PARSA, M. R. & WAGNER, A. J. 2020 Large fluctuations in nonideal coarse-grained systems. *Phys. Rev. Lett.* **124** (23), 234501.
- PELUSI, F., SBRAGAGLIA, M., BENZI, R., SCAGLIARINI, A., BERNASCHI, M. & SUCCI, S. 2021 Rayleigh-Bénard convection of a model emulsion: anomalous heat-flux fluctuations and finite-size droplet effects. *Soft Matter* **17** (13), 3709–3721.
- PENG, D. Y. & ROBINSON, D. B. 1976 A new two-constant equation of state. *Ind. Eng. Chem. Fundam.* **15** (1), 59–64.
- PERLEKAR, P., BENZI, R., CLERCX, H. J. H., NELSON, D. R. & TOSCHI, F. 2014 Spinodal decomposition in homogeneous and isotropic turbulence. *Phys. Rev. Lett.* **112** (1), 014502.
- PERSAD, A. H. & WARD, C. A. 2016 Expressions for the evaporation and condensation coefficients in the hertz-knudsen relation. *Chem. Rev.* **116**, 7727–7767.
- PHILIPPI, P. C., HEGELE, L. A., DOS SANTOS, L. O. E. & SURMAS, R. 2006 From the continuous to the lattice Boltzmann equation: The discretization problem and thermal models. *Phys. Rev. E* **73** (5), 056702.
- QIN, F., DEL CARRO, L., MAZLOOMI MOQADDAM, A., KANG, Q., BRUNSCHWILER, T.,

- DEROME, D. & CARMELIET, J. 2019 Study of non-isothermal liquid evaporation in synthetic micro-pore structures with hybrid lattice Boltzmann model. *J. Fluid Mech.* **866**, 33–60.
- QIU, R., BAO, Y., ZHOU, T., CHE, H., CHEN, R. & YOU, Y. 2020 Study of regular reflection shock waves using a mesoscopic kinetic approach: Curvature pattern and effects of viscosity. *Phys. Fluids* **32** (10), 106106.
- QIU, R., ZHOU, T., BAO, Y., ZHOU, K., CHE, H. & YOU, Y. 2021 Mesoscopic kinetic approach for studying nonequilibrium hydrodynamic and thermodynamic effects of shock wave, contact discontinuity, and rarefaction wave in the unsteady shock tube. *Phys. Rev. E* **103** (5), 053113.
- RANA, A. S., SAINI, S., CHAKRABORTY, S., LOCKERBY, D. A. & SPRITTLES, J. E. 2021 Efficient simulation of non-classical liquid-vapour phase-transition flows: a method of fundamental solutions. *J. Fluid Mech.* **919**.
- RASIN, I., MILLER, W. & SUCCI, S. 2005 Phase-field lattice kinetic scheme for the numerical simulation of dendritic growth. *Phys. Rev. E* **72** (6), 066705.
- REDLICH, O. & KWONG, J. N. S. 1949 On the thermodynamics of solutions. V. An equation of state. Fugacities of gaseous solutions. *Chem. Rev.* **44** (1), 233–244.
- REN, Q. 2019 Enhancement of nanoparticle-phase change material melting performance using a sinusoidal heat pipe. *Energy Convers. Manag.* **180**, 784–795.
- ROJAS, R., TAKAKI, T. & OHNO, M. 2015 A phase-field-lattice Boltzmann method for modeling motion and growth of a dendrite for binary alloy solidification in the presence of melt convection. *J. Comput. Phys.* **298**, 29–40.
- RYKOV, V. A. 1975 A model kinetic equation for a gas with rotational degrees of freedom. *Fluid Dyn.* **10** (6), 959–966.
- SAFARI, H., RAHIMIAN, M. H. & KRAFCZYK, M. 2013 Extended lattice Boltzmann method for numerical simulation of thermal phase change in two-phase fluid flow. *Phys. Rev. E* **88** (1), 013304.
- SAFARI, H., RAHIMIAN, M. H. & KRAFCZYK, M. 2014 Consistent simulation of droplet evaporation based on the phase-field multiphase lattice Boltzmann method. *Phys. Rev. E* **90** (3), 033305.
- SBRAGAGLIA, M., BENZI, R., BIFERALE, L., SUCCI, S., SUGIYAMA, K. & TOSCHI, F. 2007 Generalized lattice Boltzmann method with multirange pseudopotential. *Phys. Rev. E* **75** (2), 026702.
- SBRAGAGLIA, M. & SUCCI, S. 2005 Analytical calculation of slip flow in lattice Boltzmann models with kinetic boundary conditions. *Phys. Fluids* **17** (9), 093602.
- SCHWEIZER, M., ÖTTINGER, H. C. & SAVIN, T. 2016 Nonequilibrium thermodynamics of an interface. *Phys. Rev. E* **93** (5), 052803.
- SHAKHOV, E. M. 1968 Generalization of the krook kinetic relaxation equation. *Fluid Dyn.* **3** (5), 95–96.
- SHAN, X. & CHEN, H. 1993 Lattice Boltzmann model for simulating flows with multiple phases and components. *Phys. Rev. E* **47** (3), 1815–1819.
- SHAN, X. & CHEN, H. 1994 Simulation of nonideal gases and liquid-gas phase transitions by the lattice Boltzmann equation. *Phys. Rev. E* **49** (4), 2941–2948.
- SHAN, X., YUAN, X. & CHEN, H. 2006 Kinetic theory representation of hydrodynamics: a way beyond the Navier-Stokes equation. *J. Fluid Mech.* **550**, 413–441.

- SHI, B. & GUO, Z. 2009 Lattice Boltzmann model for nonlinear convection-diffusion equations. *Phys. Rev. E* **79** (1), 016701.
- SHI, Y. & SHAN, X. 2021 A multiple-relaxation-time collision model for nonequilibrium flows. *Phys. Fluids* **33** (3), 037134.
- SHI, Y., WU, L. & SHAN, X. 2021 Accuracy of high-order lattice Boltzmann method for non-equilibrium gas flow. *J. Fluid Mech.* **907**, A25.
- SOFONEA, V., BICIUȘCĂ, T., BUSUIOC, S., AMBRUȘ, VICTOR E, GONNELLA, G & LAMURA, A 2018 Corner-transport-upwind lattice Boltzmann model for bubble cavitation. *Phys. Rev. E* **97** (2), 023309.
- SOFONEA, V., LAMURA, A., GONNELLA, G. & CRISTEA, A. 2004 Finite-difference lattice Boltzmann model with flux limiters for liquid-vapor systems. *Phys. Rev. E* **70** (4), 046702.
- SOFONEA, V. & SEKERKA, R. F. 2005 Diffuse-reflection boundary conditions for a thermal lattice Boltzmann model in two dimensions: Evidence of temperature jump and slip velocity in microchannels. *Phys. Rev. E* **71** (6), 066709.
- STANLEY, H. E. 1971 *Phase transitions and critical phenomena*. Clarendon Press, Oxford.
- STRUCHTRUP, H. 1997 The BGK-model with velocity-dependent collision frequency. *Continuum Mech. Thermodyn.* **9** (1), 23–31.
- STRUCHTRUP, H. 2005 *Macroscopic Transport Equations for Rarefied Gas Flows: Approximation Methods in Kinetic Theory*. Springer, Heidelberg.
- STRUCHTRUP, H., BECKMANN, A., RANA, A. S. & FREZZOTTI, A. 2017 Evaporation boundary conditions for the r13 equations of rarefied gas dynamics. *Phys. Fluids* **29** (9), 092004.
- STRUCHTRUP, H. & FREZZOTTI, A. 2022 Twenty-six moment equations for the enskog-vlasov equation. *J. Fluid Mech.* **940**.
- STRUCHTRUP, H. & TORRILHON, M. 2003 Regularization of Grad's 13 moment equations: Derivation and linear analysis. *Phys. Fluids* **15** (9), 2668–2680.
- SU, X. & LIN, C. 2022 Nonequilibrium effects of reactive flow based on gas kinetic theory. *Comm. Theor. Phys.* **74** (3), 035604.
- SUCCI, SAURO 2001 *The lattice Boltzmann equation: for fluid dynamics and beyond*. Oxford University Press.
- SUCCI, S. 2014 A note on the lattice Boltzmann versus finite-difference methods for the numerical solution of the Fisher's equation. *Int. J. Mod. Phys. C* **25** (01), 1340015.
- SUCCI, S. 2018 *The Lattice Boltzmann Equation: For Complex States of Flowing Matter*. Oxford University Press.
- SUCCI, S., AMATI, G., BONACCORSO, F., LAURICELLA, M., BERNASCHI, M., MONTESSORI, A. & TIRIBOCCHI, A. 2020 Toward exascale design of soft mesoscale materials. *J. Comput. Sci.* **46**, 101175.
- SUCCI, S., MONTESSORI, A., LAURICELLA, M., TIRIBOCCHI, A. & BONACCORSO, F. 2021 Density functional kinetic theory for soft matter. *Proc. SIMAI 2020+* **21** .
- SUN, D., PAN, S., HAN, Q. & SUN, B. 2016a Numerical simulation of dendritic growth in directional solidification of binary alloys using a lattice Boltzmann scheme. *Int. J. Heat Mass Transfer* **103**, 821–831.
- SUN, D., ZHU, M., WANG, J. & SUN, B. 2016b Lattice Boltzmann modeling of bubble formation and dendritic growth in solidification of binary alloys. *Int. J. Heat Mass Transfer* **94**, 474–487.
- SWIFT, M. R., ORLANDINI, E., OSBORN, W. R. & YEOMANS, J. M. 1996 Lattice Boltzmann simulations of liquid-gas and binary fluid systems. *Phys. Rev. E* **54** (5), 5041–5052.

- SWIFT, M. R., OSBORN, W. R. & YEOMANS, J. M. 1995 Lattice Boltzmann simulation of nonideal fluids. *Phys. Rev. Lett.* **75** (5), 830–833.
- TAVARES, H. S., BIFERALE, L., SBRAGAGLIA, M. & MAILYBAEV, A. A. 2021 Immiscible rayleigh-taylor turbulence using mesoscopic lattice Boltzmann algorithms. *Phys. Rev. Fluids* **6** (5), 054606.
- TIAN, Y., LIU, X., ZHENG, H., XU, Q., ZHU, Z., LUO, Q., SONG, C., GAO, K., YAO, H., DANG, C. & XUAN, Y. 2022 Artificial mitochondrion for fast latent heat storage: Experimental study and lattice Boltzmann simulation. *Energy* p. 123296.
- TORRILHON, M. 2016 Modeling nonequilibrium gas flow based on moment equations. *Annu. Rev. Fluid Mech.* **48**, 429–458.
- TOSCHI, F. & SUCCI, S. 2005 Lattice Boltzmann method at finite knudsen numbers. *EPL* **69** (4), 549.
- VILAR, J. M. G. & RUBI, J. M. 2001 Thermodynamics “beyond” local equilibrium. *Proc. Natl. Acad. Sci.* **98** (20), 11081–11084.
- WAGNER, A. J. 2003 The origin of spurious velocities in lattice Boltzmann. *Int. J. Mod. Phys. C* **17** (01n02), 193–196.
- WAGNER, A. J. 2006 Thermodynamic consistency of liquid-gas lattice boltzmann simulations. *Phys. Rev. E* **74** (5), 056703.
- WAGNER, A. J. & PAGONABARRAGA, I. 2002 Lees-Edwards boundary conditions for lattice Boltzmann. *J. Stat. Phys.* **107** (1), 521–537.
- WAGNER, A. J., WILSON, L. M. & CATES, M. E 2003 Role of inertia in two-dimensional deformation and breakdown of a droplet. *Phys. Rev. E* **68** (4), 045301.
- WAGNER, A. J. & YEOMANS, J. M. 1998 Breakdown of scale invariance in the coarsening of phase-separating binary fluids. *Phys. Rev. Lett.* **80** (7), 1429.
- WANG, C., XU, A., ZHANG, G. & LI, Y. 2009 Simulating liquid-vapor phase separation under shear with lattice boltzmann method. *Sci. China, Ser. G* **52** (9), 1337–1344.
- WANG, H. 2017a Numerical simulation for the solitary wave of Zakharov-Kuznetsov equation based on lattice Boltzmann method. *Appl. Math. Model.* **45**, 1–13.
- WANG, H. 2017b Solitary wave of the Korteweg-de Vries equation based on lattice Boltzmann model with three conservation laws. *Adv. Space Res.* **59** (1), 283–292.
- WANG, H. 2019 Numerical simulation for solitary wave of Klein-Gordon-Zakharov equation based on the lattice Boltzmann model. *Comput. Math. Appl.* **78** (12), 3941–3955.
- WANG, H. 2020 Numerical simulation for (3+ 1) d solitary wave of extended zakharov-kuznetsov equation in dusty plasma based on lattice Boltzmann method. *Phys. Lett. A* **384** (32), 126809.
- WANG, H., LI, X., LI, Y. & GENG, X. 2017 Simulation of phase separation with large component ratio for oil-in-water emulsion in ultrasound field. *Ultrason. Sonochem.* **36**, 101–111.
- WANG, Y., SHU, C., HUANG, H. B. & TEO, C. J. 2015a Multiphase lattice Boltzmann flux solver for incompressible multiphase flows with large density ratio. *J. Comput. Phys.* **280**, 404–423.
- WANG, Y., SHU, C. & YANG, L. 2015b An improved multiphase lattice Boltzmann flux solver for three-dimensional flows with large density ratio and high Reynolds number. *J. Comput. Phys.* **302**, 41–58.
- WATARI, M. 2016 Is the lattice Boltzmann method applicable to rarefied gas flows? Comprehensive evaluation of the higher-order models. *J. Fluids Eng.* **138** (1).

- WEEKS, J. D. 1977 Structure and thermodynamics of the liquid-vapor interface. *J. Chem. Phys.* **67** (7), 3106–3121.
- WEI, Y., LI, Y., WANG, Z., YANG, H., ZHU, Z., QIAN, Y. & LUO, K. H. 2022 Small-scale fluctuation and scaling law of mixing in three-dimensional rotating turbulent Rayleigh-Taylor instability. *Phys. Rev. E* **105** (1), 015103.
- WEN, B., ZHAO, L., QIU, W., YE, Y. & SHAN, X. 2020 Chemical-potential multiphase lattice Boltzmann method with superlarge density ratios. *Phys. Rev. E* **102** (1), 013303.
- WEN, B., ZHOU, X., HE, B., ZHANG, C. & FANG, H. 2017 Chemical-potential-based lattice Boltzmann method for nonideal fluids. *Phys. Rev. E* **95** (6), 063305.
- WÖHRWAG, M., SEMPREBON, C., MAZLOOMI MOQADDAM, A., KARLIN, I. & KUSUMAATMAJA, H. 2018 Ternary free-energy entropic lattice Boltzmann model with a high density ratio. *Phys. Rev. Lett.* **120** (23), 234501.
- WU, J. L., LI, Z. H., ZHANG, Z. B. & PENG, A. P. 2021a On derivation and verification of a kinetic model for quantum vibrational energy of polyatomic gases in the gas-kinetic unified algorithm. *J. Comput. Phys.* **435**, 109938.
- WU, W., LIU, Q. & WANG, B. 2021b Curved surface effect on high-speed droplet impingement. *J. Fluid Mech.* **909**, A7.
- XU, A., CHEN, J., SONG, J., CHEN, D. & CHEN, Z. 2021a Progress of discrete Boltzmann study on multiphase complex flows. *Acta Aerodyn. Sin.* **39** (3), 138–169.
- XU, A., GONNELLA, G. & LAMURA, A. 2003 Phase-separating binary fluids under oscillatory shear. *Phys. Rev. E* **67** (5), 056105.
- XU, A., GONNELLA, G. & LAMURA, A. 2004 Numerical study of the ordering properties of lamellar phase. *Physica A* **344** (3-4), 750–756.
- XU, A., SHAN, Y., CHEN, F., GAN, Y. & LIN, C. 2021b Progress of mesoscale modeling and investigation of combustion multi-phase flow. *Acta Aeronaut. Astronaut. Sin.* **42** (12), 625842.
- XU, A., SONG, J., CHEN, F., XIE, K. & YING, Y. 2021c Modeling and analysis methods for complex fields based on phase space. *Chinese J. Comput. Phys.* **38** (6), 631.
- XU, A., ZHANG, G. & ZHANG, Y. 2018 *Kinetic Theory Chap. 02*. edited by Kyzas, G. and Mitropoulos, A., InTech.
- XU, A. G., ZHANG, G. C., GAN, Y. B., CHEN, F. & YU, X. J. 2012 Lattice Boltzmann modeling and simulation of compressible flows. *Front. Phys.* **7** (5), 582–600.
- XU, X., CHEN, Y. & XU, K. 2021d Modeling and computation for non-equilibrium gas dynamics: Beyond single relaxation time kinetic models. *Phys. Fluids* **33** (1), 011703.
- YAN, G. 2000 A lattice Boltzmann equation for waves. *J. Comput. Phys.* **161** (1), 61–69.
- YAN, W., CAI, B., LIU, Y. & FU, B. 2012 Effects of wall shear stress and its gradient on tumor cell adhesion in curved microvessels. *Biomech. Model. Mechan.* **11** (5), 641–653.
- YANG, L. M., SHU, C., YANG, W. M., CHEN, Z. & DONG, H. 2018 An improved discrete velocity method (DVM) for efficient simulation of flows in all flow regimes. *Phys. Fluids* **30** (6), 062005.
- YANG, Y., SHAN, M., KAN, X., SHANGGUAN, Y. & HAN, Q. 2020 Thermodynamic of collapsing cavitation bubble investigated by pseudopotential and thermal MRT-LBM. *Ultrason. Sonochem.* **62**, 104873.
- YANG, Y., SHAN, M., SU, N., KAN, X., Y., SHANGGUAN & HAN, Q. 2022 Role of wall temperature on cavitation bubble collapse near a wall investigated using thermal lattice Boltzmann method. *Int. Commun. Heat Mass Transfer* **134**, 105988.

- ZHANG, D. 2020 *Acoustic Levitation: From Physics to Applications*. Springer Nature.
- ZHANG, D., TARAFDAR, S., TARASEVICH, Y. Y., CHOUDHURY, M. D. & DUTTA, T. 2019 Evaporation of a droplet: From physics to applications. *Phys. Rep.* **804**, 1–56.
- ZARGHAMI, A. & VAN DEN AKKER, H. E. A. 2017 Thermohydrodynamics of an evaporating droplet studied using a multiphase lattice Boltzmann method. *Phys. Rev. E* **95** (4), 043310.
- ZHANG, D., XU, A., ZHANG, Y., GAN, Y. & LI, Y. 2022a Discrete Boltzmann modeling of high-speed compressible flows with various depths of non-equilibrium. *arXiv preprint arXiv:2205.13809* .
- ZHANG, D., XU, A., ZHANG, Y. & LI, Y. 2020 Two-fluid discrete Boltzmann model for compressible flows: Based on ellipsoidal statistical Bhatnagar-Gross-Krook. *Phys. Fluids* **32** (12), 126110.
- ZHANG, G., XU, A., ZHANG, D., LI, Y., LAI, H. & HU, X. 2021 Delineation of the flow and mixing induced by Rayleigh-Taylor instability through tracers. *Phys. Fluids* **33** (7), 076105.
- ZHANG, J. & YAN, G. 2010 Lattice Boltzmann model for the complex Ginzburg-Landau equation. *Phys. Rev. E* **81** (6), 066705.
- ZHANG, J. & YAN, G. 2014 Three-dimensional lattice Boltzmann model for the complex Ginzburg-Landau equation. *J. Sci. Comput.* **60** (3), 660–683.
- ZHANG, J., YAN, G. & DONG, Y. 2009 A new lattice Boltzmann model for the Laplace equation. *Appl. Math. Comput.* **215** (2), 539–547.
- ZHANG, R., HE, X., DOOLEN, G. & CHEN, S. 2001 Surface tension effects on two-dimensional two-phase Kelvin-Helmholtz instabilities. *Adv. Water Res.* **24** (3-4), 461–478.
- ZHANG, R., SHAN, X. & CHEN, H. 2006 Efficient kinetic method for fluid simulation beyond the Navier-Stokes equation. *Phys. Rev. E* **74** (4), 046703.
- ZHANG, Y., XU, A., CHEN, F., LIN, C. & WEI, Z. H. 2022b Non-equilibrium characteristics of mass and heat transfers in the slip flow. *AIP Adv.* **12** (3), 035347.
- ZHANG, Y., XU, A., ZHANG, G., GAN, Y., CHEN, Z. & SUCCI, S. 2019 Entropy production in thermal phase separation: a kinetic-theory approach. *Soft Matter* **15** (10), 2245–2259.
- ZHANG, Y., XU, A., ZHANG, G., ZHU, C. & LIN, C. 2016 Kinetic modeling of detonation and effects of negative temperature coefficient. *Combustion and Flame* **173**, 483–492.
- ZHENG, H. W., SHU, C. & CHEW, Y. T. 2006 A lattice Boltzmann model for multiphase flows with large density ratio. *J. Comput. Phys.* **218** (1), 353–371.